Water Resources Research

RESEARCH ARTICLE
10.1029/2025WR041287

Capturing Non-Fickian Mesoscale Solute Transport in Porous Media: The Role of Transient Storage and Mass Exchange

Prasanjaya Ekanayake[1], Mariaines Di Dato[1], Daniele Tonina[2], and Alberto Bellin[1,3]

[1]Department of Civil, Environmental and Mechanical Engineering, University of Trento, Trento, Italy, [2]Department of Civil & Environmental Engineering, Center for Ecohydraulics Research, University of Idaho, Boise, ID, USA, [3]C3A - Center Agriculture Food Environment, University of Trento, Trento, Italy

Key Points:

- Mesoscale experiments show breakthrough curve long-tails due to heterogeneity in pore-scale velocity and transient storage
- Solute delay in transient storage zones is a key process to explain non-Fickian behavior at the mesoscale
- Theoretical dispersivity model aligns with experiments when paired with transient storage

Supporting Information:

Supporting Information may be found in the online version of this article.

Correspondence to:

A. Bellin,
alberto.bellin@unitn.it

Citation:

Ekanayake, P., Di Dato, M., Tonina, D., & Bellin, A. (2026). Capturing non-Fickian mesoscale solute transport in porous media: The role of transient storage and mass exchange. *Water Resources Research*, *62*, e2025WR041287. https://doi.org/10.1029/2025WR041287

Received 9 JUN 2025
Accepted 6 FEB 2026

Abstract Solute transport in porous media at the mesoscale, whose characteristic dimension is in the range of tens to hundreds of grain diameters, is governed by disordered pore-scale velocity fields, often producing a non-Fickian behavior that cannot be described by the classical Advection–Dispersion Equation (ADE) with constant dispersivity. We investigate this behavior using transport experiments in hydrogel bead media, combining planar laser-induced fluorescence and refractive index matching to obtain high-resolution tracer concentration data across a control plane. The resulting breakthrough curves (BTCs) exhibit long tailing, a sign of non-Fickian transport. To interpret the experimental results, we developed a stochastic model of the BTC at the control plane, considering both constant (Fickian) and time-varying dispersivity derived from theory. For the time-varying case, we used the macrodispersion stochastic model developed for heterogeneous formations. The Fickian limit was set using the analytical expression for spherical inclusions in uniform fluid flow, which was also applied to the constant dispersivity model. Both parameterizations capture the bulk of the BTC but fail to reproduce the tail. By incorporating a mobile–immobile mass exchange model to account for solute retention in low-velocity and stagnant zones, we achieved excellent agreement across the entire BTC with the analytical expressions of dispersivity. The fitted exchange parameters resulted in low Damköhler numbers, which confirm significant delay of a small portion of the injected mass as epitomized by slow exchange. These results underscore the importance of including transient storage processes in mesoscale transport models to predict BTC tailing and retention accurately.

Plain Language Summary When water carries a solute through porous materials—like soil, filters, or biological tissues—its movement is often more complex than predicted by the classical Advection–Dispersion Equation, which assumes constant dispersion. A key sign of this complexity is the slow decay in the time series of solute concentration at an observation device, where small amounts of solute continue to arrive long after the bulk of the plume has passed. In this study, we investigated this behavior at laboratory (mesoscale) conditions, using transparent beads of uniform size to build a porous medium. We used a laser-based imaging method to track the movement of a dye tracer across a control plane. Our results showed clear long-tailing, consistent with anomalous transport. We interpreted the data using a model that combines dispersivity, based on bead size, with a mobile–immobile exchange process that accounts for stagnant and low-flow regions. This approach successfully reproduced the full time series of solute concentration. Our findings show that even at small scales, exchange between flowing and stagnant regions affects solute migration through porous media. These processes should be included in models used to predict solute transport in both natural and engineered systems.

1. Introduction

Solute transport in porous media is a fundamental process governing a wide range of natural and engineered systems across multiple scales. In geological formations and at the field scale (from meters to kilometers), solute transport is commonly modeled using the Darcian approach, where hydraulic properties are homogenized over a Representative Elementary Volume (REV) several hundred times larger than the mean pore size (Bear, 1972; Dagan, 1989; Rubin, 2003). However, flow and transport processes at or near the REV scale, hereafter referred to as mesoscale (typically defined as a few tenths to tens of centimeters or tens to hundreds of the median diameter of the granular material), are relevant for solutes reacting upon mixing (see e.g., Basilio Hazas et al., 2022; Bertran

et al., 2023; Wright et al., 2017; Ye et al., 2015; Ziliotto et al., 2025) and in several industrial (e.g., Betancur et al., 2024; Salek et al., 2024) and biomedical applications (e.g., Alves et al., 2023; Cookson et al., 2012). This dimension is also relevant in laboratory experiments (e.g., Moroni & Cushman, 2001b; Rau et al., 2012).

In industrial applications, mesoscale transport processes control mixing in microfluidic devices (Betancur et al., 2024; Izaguirre & Parsa, 2024; Salek et al., 2024), chemical reactions and dispersion in packed-bed reactors (Edery et al., 2015; Fathiganjehlou et al., 2023), oil recovery and flow redistribution in porous media (Datta, Ramakrishnan, & Weitz, 2014; Parsa et al., 2020, 2021), and filtration efficiency in water treatment systems (Lan et al., 2022; N. Yuan et al., 2022). In biomedical applications, they are controlling factors in coronary perfusion (Alves et al., 2023; Cookson et al., 2012), drug delivery (Varghese et al., 2014; Verma et al., 2021), solute exchange in biological tissues and bioengineered scaffolds (Bhattacharjee & Datta, 2019; Chen & Niklason, 2012; Facchini et al., 2014; Peppas, 2000; Y. Zhang et al., 2024), as well as nutrient transport in cellular environments (Butler et al., 1997; Jia et al., 2021; T. Yuan et al., 2024; Zhao et al., 2016).

Mesoscale heterogeneity arises from variations in pore geometry (Datta et al., 2013; Foster et al., 2021), pore size (Iraji et al., 2024), and pore connectivity (W. Zhang et al., 2024; Z. Zhang et al., 2024), as well as differences in grain permeability (Koch & Brady, 1985), grain surface roughness, and chemical properties (Zakirov & Khramchenkov, 2022). The combined effect of these structural and physical features produces a heterogeneous velocity field, which is the primary driver of solute transport inhomogeneities and mixing (Dentz et al., 2018; Kitanidis, 1994; Soltanmohammadi et al., 2024).

At the mesoscale, as well as at the larger scales, transport was traditionally modeled by the classical Advection Dispersion Equation (ADE) with constant (Fickian) dispersion coefficients empirically dependent on pore size (Bear, 1972; Delgado, 2006). However, mesoscale heterogeneity leads to deviation from the classical theory of Fickian transport, leading to scale-dependent dispersion commonly known as "anomalous dispersion" (Berkowitz et al., 2000; Berkowitz & Scher, 2010; Cushman & Moroni, 2001; De Anna et al., 2017; Dentz et al., 2018; Kennedy & Lennox, 2001; Krol et al., 2021; Rolle & Kitanidis, 2014; Uffink et al., 2012). Many numerical studies, mostly two-dimensional, have complemented experimental observations by evaluating the impact of pore- and grain-scale heterogeneity on solute transport and mixing (Dyson et al., 2008; Karimi & Bhattya, 2024; Ou et al., 2024). These studies typically analyzed breakthrough curves (BTCs), which provide a macroscopic view of solute transport by recording the temporal evolution of concentration across a control plane. The analysis of BTCs has revealed long-tailing behavior indicative of anomalous transport (Berkowitz & Scher, 2010; Edery et al., 2015; Hu et al., 2024; Kasai et al., 2024; Kennedy & Lennox, 2001; Nissan & Berkowitz, 2019; Nissan et al., 2017a; Silliman, 2001). Most simulations and experiments focused on two-dimensional systems, analyzing BTCs at control planes or concentration profiles along transects perpendicular to the mean flow direction (S.-B. Kim et al., 2004; Magnico, 2003; Moradi & Mehdinejadiani, 2020; Pang et al., 2003; Rashidi et al., 1996; Silliman & Simpson, 1987; Tatti et al., 2018).

Although the influence of heterogeneity in the hydraulic properties has been extensively studied at the large (field) scale (see e.g., Berkowitz & Scher, 2010; Dagan, 1989; Fiori et al., 2015; Gelhar, 1986, 1993; Rubin, 2003), the role of mesoscale heterogeneity on solute transport remains comparatively underexplored (Berkowitz et al., 2000; Liu et al., 2024; Nissan et al., 2017b; Porta et al., 2015; Puyguiraud et al., 2021), despite its critical role in both biomedical and industrial applications, and in controlling mixing at larger scales (Ziliotto et al., 2025).

At the mesoscale, the geometrical complexity of interconnected pores leads to a disordered flow field with stagnant and recirculation zones (Basham et al., 2019; Rubol et al., 2018). These zones temporarily immobilize the solute, creating localized transient storage effects that delay solute migration (van Beinum et al., 2000; Van Beinum et al., 2000). As a result, solutes exhibit prolonged residence times, leading to non-Fickian (long) tailing in BTCs. Transient storage zones may emerge as key contributors to anomalous transport behavior, and their effect can be modeled as a mobile-immobile exchange process (Coats & Smith, 1964). A direct experimental validation of this behavior was provided by Rao et al. (1980), who demonstrated that conservative tracers exhibit long-tailed breakthrough curves due to immobile water within aggregates.

While these mechanisms are often implicit in upscaled models, their physical origin and quantitative role in laboratory-scale transport remain poorly constrained and merit further investigation. Non-Gaussian velocity fields with persistent low-velocity regions at the mesoscale were observed in a number of experimental works

performed in irregularly packed spherical beads porous medium (see e.g., Huang et al., 2008; Lachhab et al., 2008; Lebon et al., 1996). Similarly, Souzy et al. (2020) observed a highly skewed velocity distribution with low-velocity and reverse-flow zones in an index-matched spherical bead pack porous media investigated by means of three-dimensional particle-tracking velocimetry. Furthermore, Sanquer et al. (2024) used 3D laser-induced fluorescence in an index-matched bead pack (6–8 mm spheres) to study lamellar mixing and chaotic advection. They demonstrated that for a conservative tracer, the chaotic stretching and folding of dye filaments create localized regions of low mobility, thereby revealing that hydrodynamic mixing alone can produce anomalous transport features in nearly monodisperse media. These studies provided detailed pore-scale analyses that revealed the complexity of the flow field developing in an apparently regular porous medium, such as those formed by packed spherical beads. However, our understanding of how these pore-scale processes influence mesoscale transport, and our ability to model them, remains limited.

To address this knowledge gap, and building on a pioneering two-dimensional experimental study by Cenedese and Viotti (1996), further extended to three dimensions by Moroni and Cushman (2001a) and Moroni et al. (2007), we conducted three-dimensional mesoscale solute transport experiments to investigate solute transport at the mesoscale. Our porous medium was composed of transparent hydrogel spheres with a Refraction Index Matching (RIM) that of fresh water (RI = 1) (Basham et al., 2019; Budwig, 1994; Datta, Dupin, & Weitz, 2014; Datta & Weitz, 2013; Rubol et al., 2018). When the solid refraction index matches that of the working fluid, the light passes through it without being reflected or refracted when immersed in the fluid. RIM enables the use of non-invasive optical techniques such as Planar Laser-Induced Fluorescence (PLIF) or Particle Image Velocimetry (PIV) to map concentration or flow fields (Basham et al., 2019; Budwig, 1994; Hilliard et al., 2023; Naftaly et al., 2015; Rubol et al., 2018). Unlike previous studies that used Pyrex spheres and glycerol as fluid (Cenedese & Viotti, 1996; Moroni & Cushman, 2001a), the use of hydrogel spheres allowed us to use deionized water, which is easier to handle than glycerol (noting that glycerol has a density and viscosity very different from water) and has physical properties closer to the environmental conditions. By coupling RIM with PLIF, we mapped the spatial and temporal concentration distributions of Rhodamine B, used as a conservative fluorescent tracer. This experimental approach provides a high-resolution view of solute transport in a three-dimensional porous medium at the mesoscale. We were able to identify that the formation of transient storage zones is a key process controlling the long tail of the BTCs at the mesoscale.

We interpreted the experimental results by using a stochastic Lagrangian model with particle displacement represented as a correlated random walk. This model shares conceptual similarities with the Lagrangian framework developed for solute transport in heterogeneous field-scale porous formations (e.g., Dagan, 1989; Gelhar, 1993; Gelhar & Axness, 1983; Rubin, 2003). The stochastic theory of transport by continuous movement was able to capture the bulk BTC, but the tail was captured only after including a transient storage model.

2. Material and Methods

2.1. Laboratory Experiments

The experimental setup consisted of a cell of transparent Plexiglas walls 17 cm tall with a 9 cm squared base, a green laser light to illuminate the control plane at which the distribution of solute concentration is measured, and a high-resolution camera (Figure 1a).

The cell was filled with hydrogel spheres of uniform diameter to obtain a synthetic porous medium, and the experiments were conducted with two diameters: $d = 10$ mm and $d = 15$ mm (Figure 1c). Dried hydrogel spheres were first hydrated in deionized water for 12 hr to achieve the final diameter and mechanical strength. The hydrated hydrogel beads were carefully placed randomly inside the experimental cell, resulting in a non-uniform and non-periodic (heterogeneous) distribution of the voids (Turuban et al., 2018). The sample was then saturated by gradually adding the same deionized water used to hydrate the hydrogel spheres, with attention to avoid air bubble entrapment. Soft granular materials such as hydrogel may deform under fluid-induced stresses (MacMinn et al., 2015, 2016). However, this should not be overstated when flow is slow, given that Iskander et al. (2015) reported compression indexes in the range $0.1 \div 0.15$ for hydrogel spheres, similar to the values typical of silt. This makes hydrogel beads a suitable material for flow and transport experiments at the mesoscale, without compromising the mechanical stability of the medium.

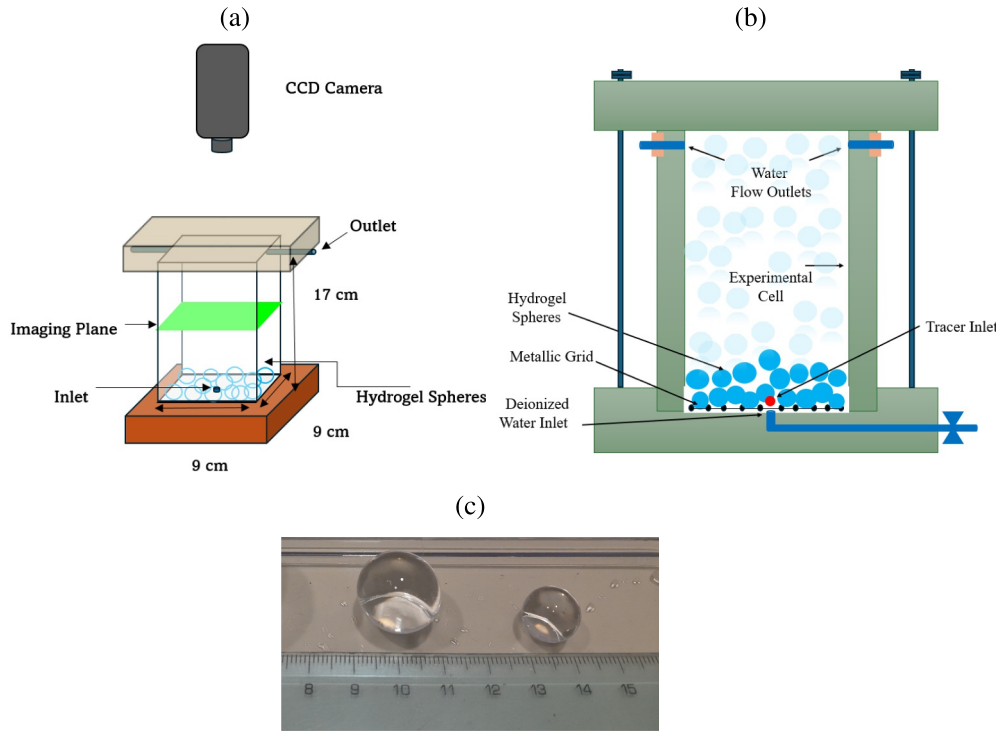

Figure 1. (a) Schematic of the experimental setup, highlighting the Planar Laser-Induced Fluorescence arrangement with its key components used for monitoring Rhodamine B dispersion within the cell. (b) Schematic 2D cross-section of the experimental cell. (c) Photograph of two representative hydrogel grains (with diameters d = 15 and 10 mm) used in the experiments.

In the experimental setup, deionized water flows into the hydrogel matrix from the center of the cell bottom as a point inlet. A thin metallic grid is placed at the cell bottom to support the hydrogel spheres and prevent them from obstructing the water inlet, as sketched in Figure 1b. The tracer injection port is positioned about 1 mm above the cell bottom. It lies directly over the deionized water inlet and immediately above the metallic grid. The metallic grid is in direct contact with the bead packing, leaving no cavity or free space beneath it. As a result, the tracer from the injection port enters the porous medium immediately.

The deionized water is fed from a tank set at a level higher than the experimental cell outlets. The water level in this tank was kept constant to ensure a constant flow during the experiment. Outflow water was collected in a graduated beaker used to measure the volumetric flow, which was kept constant during the experiment. Rhodamine B was used as a tracer because of its high solubility in neutral pH water, bright fluorescence, and suitability for PLIF imaging. Its diffusion coefficient ($D_m = 10^{-9}$ m^2/s) and high molar absorption allowed precise tracking of solute transport through the porous media.

The imaging system employed a Q-switched Nd-YAG laser (532 nm, 200 mJ pulse energy) to form the horizontal laser sheet crossing the cell where images of the solute concentrations were taken. The control plane was at a distance of 0.104 m from the base of the cell. The Dantec Dynamics image acquisition unit, integrated with the software DynamicStudio (Dantec Dynamics A/S, 2021) for synchronized image capture, was employed for high-resolution image acquisition. Dantec FlowSense-EO 9M-17 CCD camera, synchronized with the laser via a pulse-delay generator, captured high-resolution images at a two-second time interval. A band-pass optical filter with a central wavelength of 550 nm (±10 nm), and a cylindrical lens ensured uniform illumination and isolated fluorescent emissions, while a high-resolution lens (aperture f/2.3) produced clear and high-quality images (Figure 2). To eliminate interference, natural light sources were turned off, enabling precise visualization of tracer distribution under laser illumination. The concentration versus PLIF intensity curve was obtained by elaborating with the Dantec Dynamics system images of six well-mixed solutions prepared with known Rhodamine B concentrations.

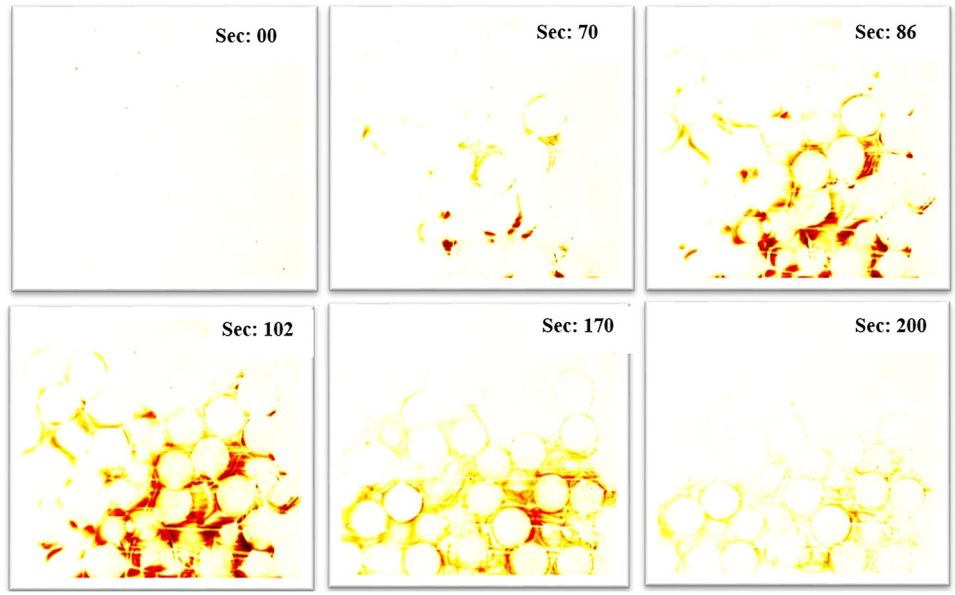

Figure 2. Sequence of Planar Laser-Induced Fluorescence images showing the spatial distribution of Rhodamine B tracer at times $t = 0$, 70, 86, 102, 170, and 200 s after experiment initiation. Images are calibrated for accurate concentration quantification and illustrate the evolving tracer dispersion and mixing dynamics in the fluid medium.

The experiments were performed by injecting a pulse of Rhodamine B solution prepared with the same deionized water flowing through the cell. The injection point was at the center of the cross-sectional plane, located $x_1 = 0.104$ m below the control plane. The pulse duration was $t_p = 16$ s for the experiment with 10 mm hydrogel spheres and $t_p = 24$ s for the experiment with 15 mm hydrogel spheres. Table 1 shows key quantities of the experiments. The porosity n was calculated by dividing the volume of voids—estimated as the volume of deionized water that needs to be added to fully saturate the sample after the placement of the saturated spheres—by the total sample volume, resulting in $n = 0.34$ and 0.39 for 10 and 15 mm hydrogel spheres, respectively. The mean velocity was then estimated as $U_{\text{exp}} = V/(n\, t_{\text{exp}}\, A)$, where V is the volume of water collected during the experiment of duration t_{exp}, and A is the cell cross-sectional area.

Solute breakthrough curves (BTCs) of the resident concentration were obtained by spatially averaging the concentration distributions within the control plane. The concentration was computed only within the pores after masking the surface occupied by the hydrogel spheres. The experimental BTCs were interpreted with the models outlined in Section 2.2. The analysis was performed with tailored software written in Python, and using the libraries scipy.special and scipy.optimize (Di Dato et al., 2025; Van Rossum & Drake, 2009; Virtanen et al., 2020). Notice that the BTCs considered here are for the resident concentration, thereby requiring the revision of the BTC theoretical models available in the literature, which have been developed for flux concentration, as described in Section 2.2. The models consider solute under two primary assumptions: (a) conservative transport "tracer" governed by the advection-dispersion equation, and (b) active solute incorporating both advection-dispersion and a mobile-immobile exchange process within the porous media. To the best of our knowledge, no experimental data exist on the sorption of Rhodamine B onto hydrogel spheres. Therefore, we performed an independent batch sorption test to verify that Rhodamine B behaves as a conservative tracer in our system. The full experimental procedure is described in Supporting Information S1. Dispersion was modeled either with the classical Fickian approach or by accounting for medium heterogeneity through the stochastic model proposed by Dagan (1989) for transport in heterogeneous formations at the field scale.

Table 1
Key Quantities for the Two Experimental Setups

	Hydrogel spheres	
Property	$d = 10$ mm	$d = 15$ mm
Volume of water collected, V (mL)	2,012	1,770
Test duration, t_{exp} [min (s)]	10.15 (609)	12.25 (735)
Porosity, n (−)	0.34	0.39
Calculated mean velocity, U_{exp} (m/s)	0.00119	0.000762
Cross-sectional area, A (m^2)	8.1×10^{-3}	8.1×10^{-3}
Injected mass, M (g)	2.5×10^{-5}	2.5×10^{-5}
Pulse duration, t_p (s)	16	24

Note. The reported quantities include geometric properties, flow conditions, and bulk characteristics of the two synthetic porous media.

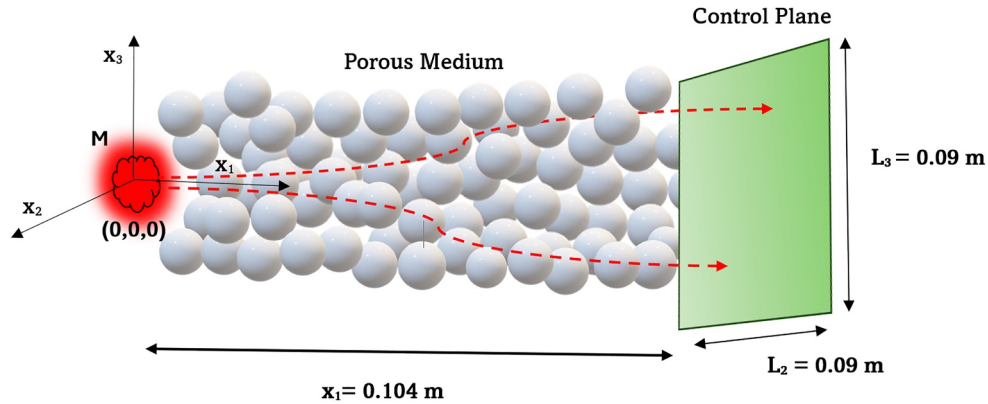

Figure 3. Schematic of the solute tracer pulse injection at location $\mathbf{a} = (0,0,0)$, with the control plane S at the distance x_1 downstream from the injection point.

2.2. Theoretical Framework of the BTC Model

In this section, we present the mathematical model used to analyze the experimental BTCs. The model accounts for three transport mechanisms: advection, hydrodynamic dispersion including molecular diffusion, and solute exchange with low velocity and immobile zones created by local heterogeneity at the pore space.

We consider the transport of a passive tracer injected at a point $\mathbf{a}$ into a heterogeneous three-dimensional flow field (Figure 3). The longitudinal distance is taken along the mean flow direction (the vertical direction in our experiments), and the information on the concentration distribution is analyzed at a control plane at a distance x_1 from the injection point. Following the Lagrangian framework, the total injected mass M is divided into a large number of non-interacting particles transported by the velocity field and subjected to molecular diffusion. Accordingly, the contribution of a particle to the concentration at the position $\mathbf{x} = (x_1, x_2, x_3)$ is given by Dagan (1987):

$$\Delta C(\mathbf{x}, t; \mathbf{a}, t_0) = \frac{\Delta \dot{M}}{n} \int_0^{t_p} \delta\left[\mathbf{x} - \mathbf{X}_t(t; \mathbf{a}, t_0)\right] dt_0 \tag{1}$$

where $\mathbf{X}_t(t; \mathbf{a}, t_0)$ is the trajectory of the particle that was released at the position $\mathbf{a}$ at time t_0, $\Delta \dot{M}\left[M L^{-3} T^{-1}\right]$ is the flux of mass per unit volume of the particle, such that the total injected mass is $M = n \int_0^{t_p} \Delta \dot{M}(t_0)\, dt_0$. Hereafter, t_p indicates the duration of the pulse injection.

The mean concentration at the control plane S can be computed by integrating Equation 1 as follows:

$$C(x_1, t) = \frac{M}{t_p L_2 L_3} \int_0^{t_p} dt_0 \int_{-L_2/2}^{L_2/2} dx_2 \int_{-L_3/2}^{L_3/2} dx_3\, \delta[\mathbf{x} - \mathbf{X}_t(t; \mathbf{a}, t_0)] \tag{2}$$

In Equation 2, we assumed that the initial mass flux is uniformly distributed among the injected particles and constant during injection: $\Delta \dot{M} = M/t_p$, and finally that $\mathbf{a} = (0,0,0)$.

The trajectory of the particle is given by (Dagan, 1987):

$$\mathbf{X}_t(t; \mathbf{a}, t_0) = \int_0^t \mathbf{v}[\mathbf{X}_t(\tau, \mathbf{a}, t_0)]\, d\tau + \mathbf{X}_B(t; \mathbf{a}, t_0) \tag{3}$$

where $\mathbf{X}_B(t; \mathbf{a}, t_0)$ is the displacement due to the Brownian motion, which represents the effect of molecular diffusion, on the particle that started from $\mathbf{a}$ at time t_0. Hereafter, we consider the velocity $\mathbf{v}$ and the point concentration, C, as Random Space Functions (RFSs).

After these preparatory steps, the ensemble mean of the spatially averaged solute concentration at time t and the control plane at x_1 assumes the following expression:

$$\langle C(x_1,t)\rangle = \frac{M}{t_p L_2 L_3}\int_0^{t_p} dt_0 \int_{-L_2/2}^{L_2/2} dx_2 \int_{-L_3/2}^{L3/2} dx_3 f(x_1,x_2,x_3,t;t_0) \tag{4}$$

where f is the probability density function of the particle's displacement.

Considering that the experimental setup has reflecting barriers at the external surface of the sample and the plane $x_1 = 0$, the particle pdf can be approximated as a truncated Gaussian distribution:

$$f(\mathbf{x},t;t_0) = \varphi'_T\left[x_1, U(t-t_0), \sqrt{X_{11}(t-t_0)}\right]\prod_{i=1}^{2}\varphi_T\left[x_i, 0, \sqrt{X_{ii}(t-t_0)}\right] \tag{5}$$

where

$$\varphi'_T[x_1,\mu,\sigma] = \frac{\exp\left[-\frac{(x_1-\mu)^2}{2\,\sigma^2}\right]}{\sqrt{2\pi}\,\sigma\left[1-\frac{1}{2}\operatorname{erfc}\left[\frac{\mu}{\sqrt{2}\sigma}\right]\right]};\quad \operatorname{erfc}(z) = 1-\operatorname{erf}(z);\quad \operatorname{erf}(z) = \frac{2}{\sqrt{\pi}}\int_0^z e^{-t^2}\,dt \tag{6}$$

and

$$\varphi_T[x_i,\mu,\sigma] = \frac{\exp\left[-\frac{(x_i-\mu)^2}{2\,\sigma^2}\right]}{\sqrt{2\pi}\,\sigma\operatorname{erf}\left[\frac{L_i}{2\sqrt{2}\ \sigma}\right]},\quad i=2,3 \tag{7}$$

By replacing Equation 5 into Equation 4 we obtain:

$$\langle C(x_1,t)\rangle = \frac{M}{t_p L_2 L_3}\int_0^{t_p} dt_0\, F(x_1,t-t_0) \tag{8}$$

with

$$F(x_1,t) = \frac{1}{\sqrt{2\pi X_{11}(t-t_0)}}\exp\left[-\frac{[x_1-U(t-t_0)]^2}{2X_{11}(t-t_0)}\right]\left\{1-\frac{1}{2}\operatorname{erfc}\left[\frac{U(t-t_0)}{\sqrt{2X_{11}(t-t_0)}}\right]\right\}^{-1} \tag{9}$$

In Equations 5 and 9 U is the mean velocity and X_{11} is the variance of the longitudinal residual particle displacement, which in the classical Fickian model assumes the following expression:

$$X_{11}(t) = 2\,\alpha_L\,U\,t + 2\,D_m\,t \tag{10}$$

where $\alpha_L\,[\mathrm{L}]$ is the longitudinal hydrodynamic dispersivity and $D_m\left[\mathrm{L}^2\,\mathrm{T}^{-1}\right]$ is the molecular diffusion coefficient.

The dispersivity observed at the laboratory scale reflects the topology of the porous matrix, namely, the shape and spatial arrangement of the grains, which influence the pathways taken by fluid particles. In the present work, we utilize the following expression for the dispersivity

$$\alpha_L^{an} = 0.19\,d(1-n) \tag{11}$$

which was proposed by Eames and Bush (1999) for a porous medium composed of spherical bodies immersed in a uniform flow field. In Appendix A1 we provide additional details on the derivation of this expression.

By using a similar approach, Jankovic et al. (2003), Dagan and Fiori (2003), and Fiori et al. (2006) proposed a stochastic model of heterogeneous porous media obtained by including permeable spheres of random hydraulic conductivity into a porous matrix with uniform hydraulic conductivity equal to the effective one. This model has been developed under the continuum hypothesis, applicable to scales larger than the REV, and by following the self-consistent approach, widely used in the study of composite materials (Dagan, 1989; S. Kim & Russel, 1985). Here, we apply Equation 11, and assess its performance for impermeable packed spheres at a scale smaller than or comparable to the REV for which the continuum hypothesis does not hold.

A large body of literature (see e.g., Rubin, 2003, for a review) showed that the model (Equation 10) can be applied to mature transport at a relatively long time and under ergodic conditions. A more general stochastic solution, including the pre-Fickian regime, and valid under ergodic conditions, is the following (Dagan, 1984):

$$X_{11}(t) = 2\int_0^t (t-\tau) v_{11}(\tau)\, d\tau + 2D_m\, t \tag{12}$$

where v_{11} is the longitudinal Lagrangian velocity covariance function. The model (Equation 12) is of general validity and applies to heterogeneous velocity fields, including those developing within pore structures below the REV scale, provided that the velocity field can be statistically characterized by a covariance function. In the present work, we adopted the Lagrangian velocity covariance function (Equation A2), obtained by solving the first-order flow equation in a heterogeneous Gaussian logconductivity field, as described in the Appendix A2. The corresponding expressions for the second moment $X_{11}(t)$ and the longitudinal dispersivity $\alpha_L(t)$ as functions of time are given in Equations A3 and A4, respectively. Although the above theory was formally developed by Dagan (1984) for scales much larger than the REV and under the continuum hypothesis, it has been shown to accurately reproduce the temporal evolution of dispersion at the laboratory scale in a discontinuous medium (Cenedese & Viotti, 1996; Moroni & Cushman, 2001a).

Under the First-Order Approximation (FOA), the dispersivity asymptotically approaches the Fickian limit at large times (in the limit as time tends to infinity):

$$\alpha_L^{foa} = \lambda\, \sigma_Y^2 \tag{13}$$

where λ is a proper integral scale. In a medium composed of impervious spheres of diameter d, the directional integral scale is given by (Di Dato et al., 2016):

$$\lambda = \int_0^\infty \chi(r)\, dr = 3\, d/8 \tag{14}$$

where $\chi(r)$ is the overlapping normalized volume between two spheres with centers separated by the distance r.

By equating Equation 13 to Equation 11 and using Equation 14 we obtain the following expression of σ_Y^2 that we use in the interpretation of our experiments:

$$\sigma_Y^2 = \frac{\alpha_L^{an}}{\lambda} = \frac{0.19\, d(1-n)}{\left(\frac{3}{8}\, d\right)} = 0.507(1-n) \tag{15}$$

In the present work, we consider two models of hydrodynamic dispersion: the asymptotic Fickian model (Equation 11) and the pre-asymptotic stochastic model (Equation A4) with the integral scale λ and variance σ_Y^2 given by Equations 14 and 15, respectively. Both models depend on porosity, n, sphere diameter, d, and mean flow velocity U.

As discussed in the Introduction, the tracer can become temporarily trapped in low-velocity zones and dead-end spaces at the contacts between spheres. These trapping regions are visible in the video provided in Movie S1. The video shows a vertical plane at the center of the cell and parallel to the external vertical walls. The development of temporary accumulation zones, evidenced in the video, cannot be reproduced with the hydrodynamic model described in Appendix A1, because of the dilute media hypothesis. We model this effect by assuming that the

tracer can exist in two states: the mobile (state A) and the trapped (state B). The tracer concentration C_{im} in the trapped (immobile) state is related to the concentration C in the mobile region. From a Lagrangian perspective, this exchange process can be modeled by allowing the particle to transition between these two states, and can be demonstrated to be the Lagrangian counterpart of the following first-order exchange kinetics:

$$\frac{\partial C_{im}}{\partial t} = k_f\, C - k_r C_{im} \tag{16}$$

where $k_f\,[\mathrm{T}^{-1}]$ and $k_r\,[\mathrm{T}^{-1}]$ are the exchange rates in the forward (from mobile to immobile) and backward (from immobile to mobile) directions, respectively.

The effect of this exchange mechanism on solute transport has been modeled by Keller and Giddings (1960), Quinodoz and Valocchi (1993) and Massabó et al. (2008) by coupling the stochastic process governing particle displacement, described by Equation 3, with a stochastic representation of the residence time t_m in the mobile phase. In this conceptual model, we assumed that the mobile phase is represented by the hydrodynamic model described in the Appendix A1 under the dilute theory. Assuming that the mass is initially in the mobile phase, Quinodoz and Valocchi (1993) derived the following expressions for the ensemble mean:

$$\langle t_m \rangle = \frac{t + K_d^2 \exp[-\Gamma] t + 2K_d(1 - \exp[-\Gamma])(k_r R_d)^{-1}}{R_d(1 + K_d \exp[-\Gamma])} \tag{17}$$

and the variance:

$$\sigma^2_{t_m} = \frac{1}{(1 + \exp[-\Gamma]K_d)\,R_d^2}\left\{t^2 + \frac{6K_d(1 - \exp[-\Gamma]K_d)\,t}{k_r R_d} + \frac{K_d^3 t^2}{\exp[\Gamma]} + \frac{6K_d(K_d - 1)(1 - \exp[-\Gamma])}{k_r^2 R_d^2}\right\} - \langle t_m \rangle^2 \tag{18}$$

of the time t_m the particle spends in the mobile phase. In Equations 17 and 18 $K_d = k_f/k_r$ is the partition equilibrium coefficient, which is a measure of how the solute distributes between the mobile and immobile phases at equilibrium; $R_d = 1 + K_d$ is the retardation factor and describes how much slower the solute moves compared to the flow due to the transient storage process; and $\Gamma = k_r R_d t$.

Under such conditions, Quinodoz and Valocchi (1993) showed that the effective moment X_{11} is expressed as the sum of two terms: one accounting for advection and dispersion, and the other that incorporates the additive effect due to transient storage:

$$X^{tr}_{11}(t) = X_{11}(\langle t_m \rangle) + U^2 \sigma^2_{t_m} \tag{19}$$

The final expression for the spatially averaged solute concentration, which includes the effect of transient storage, can be calculated by substituting into Equation 8 the function F, given by Equation 9, with the following expression:

$$F^{tr}(x_1, t) = \frac{1}{\sqrt{2\pi X^{tr}_{11}(t - t_0)}} \exp\left[-\frac{[x_1 - U(\langle t_m \rangle - t_0)]^2}{2\,X^{tr}_{11}(t - t_0)}\right]\left\{1 - \frac{1}{2} erfc\left[\frac{U(\langle t_m \rangle - t_0)}{\sqrt{2\,X^{tr}_{11}(t - t_0)}}\right]\right\}^{-1} \tag{20}$$

which is obtained by replacing X_{11} with X^{tr}_{11} and t with $\langle t_m \rangle$ into Equation 9.

3. Results

The spatial distribution of the times needed to accumulate 5%, 50%, and 95% of the total mass crossing the control plane at a given position, shown in Figure 4, provides a first indication of transport heterogeneity at the mesoscale. These mass percentiles can be considered as indicators of early, bulk, and late arrivals, respectively.

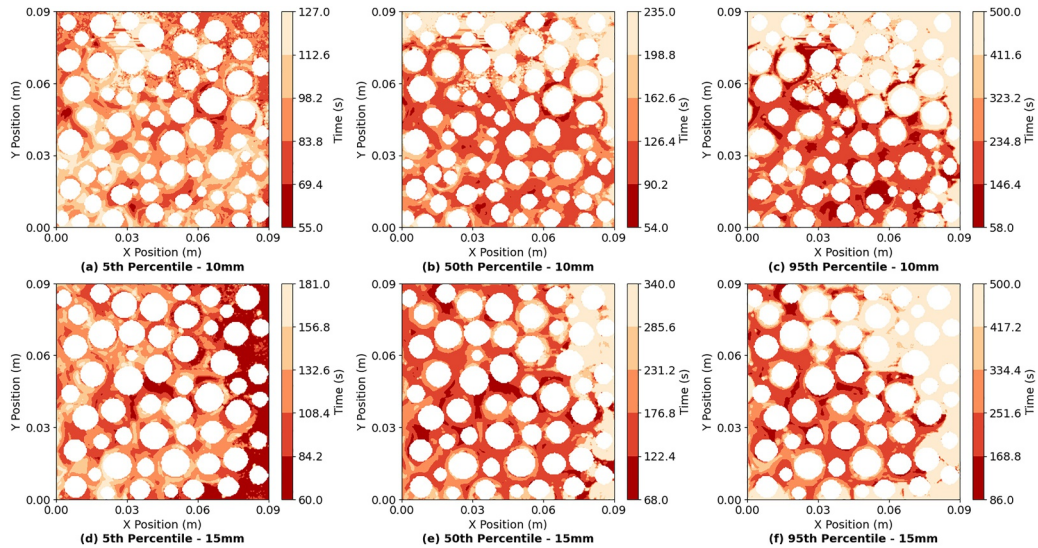

Figure 4. Spatial distribution of the accumulation time of the 5th (first column), 50th (second column) and 95th (third column) percentiles of the total accumulated mass at the control plane, for hydrogel spheres of diameters $d = 10$ mm (panels a–c) and $d = 15$ mm (panels d–f).

The spatial distribution of accumulation times in the percentile maps reveals non-uniform solute spreading. In these maps, darker regions correspond to shorter times. The arrival times of the 5th percentile mass shown in Figures 4a and 4d, which represent early arrivals, span a relatively narrow time interval over the entire control plane. A predominance of shorter arrival times is observed for the $d = 15,$mm spheres experiment near the right border of the sample (Figure 4d). We will show later that this border effect has a negligible impact on the BTC. Since the 5th percentile mass accumulation times are influenced by the velocity distribution rather than by retention effects, their heterogeneous and similar spatial distribution across the plane suggests the absence, or negligible effect, of possible tapering at the inlet. Clusters of short and long arrival times appear in the 50th and 95th percentile maps, with the latter revealing evidence of long-tailing. Interestingly, the same region showing the longest accumulation times in the 95th percentile in the $d = 15$ mm spheres case (lighter zones in Figure 4f) overlaps with the locations with prevalence of the fastest early arrivals in the 5th percentile map (darker zones in Figure 4d). This spatial overlap indirectly demonstrates the importance of exchange processes, mediated by diffusion, between zones of fast and slow velocities in addition to transient storage, and excludes the relevance of border effects in the $d = 15$ mm spheres case discussed above. This exchange mechanism is less evident, although present, in the $d = 10$ mm spheres case. The Schmidt number $Sc = Pe/Re = \mu/(\rho D_m) = 10^3$, is typical of transport processes occurring in water with relatively small molecules of solute, and it is in the range of values adopted in previous packed beds experiments (see, e.g., Elgersma et al., 2022, and the references therein). The Reynolds number $Re = \rho U\, d/\mu$, varied in the range $10.2 \div 10.7$ for $d = 10$ mm and $11.5 \div 13.6$ for $d = 15$ mm, while in the same two cases the Peclet $Pe = U\, d/D_m$ number, varied in the range $1.03 \div 1.08 \times 10^4$ and $11.5 \div 13.3 \times 10^4$, respectively (see Table 2). The high Peclet numbers indicate that transport is dominated by advection, though diffusive exchange cannot be ruled out, as will be discussed below.

Another indication of the combined effects of heterogeneity in the velocity field and transient storage with mass exchange is provided in Figures 5a and 5b. These figures show local BTCs in subareas obtained by dividing the control plane into a 3×3 grid of equal-sized square subregions. For both 10 and 15 mm sphere experiments, we observed remarkable variability in local BTCs. Notably, the maximum concentration does not occur in the central quadrant, as it would be expected for a transport process governed by the classical (Fickian) ADE with constant dispersivity. The asymmetric spatial distribution of the accumulated mass in the 9 subplanes, shown in the inset diagram, confirms that heterogeneities operating at the sub-REV scale significantly influence mass arrival at the control plane.

While such local variations may influence only marginally the bulk of the BTC of a passive tracer (e.g., at the control plane or the device outlet), they gain importance when the goal is to enhance mixing, whether in industrial

Table 2
Fitted Parameters for the Two Experiments With Porous Media Composed of Hydrogel Spheres of Diameter $d = 10$ mm and $d = 15$ mm

d [mm]	Model	Mass exchange	U [m/s]	k_f (s^{-1})	k_r (s^{-1})	Re [−]	Pe [−]
10	Fickian	No	1.026×10^{-3}	-	-	10.2	1.03×10^{4}
		Yes	1.069×10^{-3}	3.27×10^{-3}	1.12×10^{-2}	10.6	1.07×10^{4}
	Stochastic	No	1.030×10^{-3}	-	-	10.3	1.03×10^{4}
		Yes	1.076×10^{-3}	3.49×10^{-3}	1.20×10^{-2}	10.7	1.08×10^{4}
15	Fickian	No	7.72×10^{-4}	-	-	11.5	1.16×10^{4}
		Yes	8.94×10^{-4}	4.59×10^{-3}	1.96×10^{-2}	13.3	1.34×10^{4}
	Stochastic	No	7.79×10^{-4}	-	-	11.6	1.17×10^{4}
		Yes	9.09×10^{-4}	5.46×10^{-3}	2.16×10^{-2}	13.6	1.36×10^{4}

Note. In the Fickian model, we set the dispersivity α_L according to Equation 11, while in the stochastic model, we set $\lambda = 3\,d/8$ and $\sigma_Y^2 = 8\,\alpha_L^{an}/(3\,d) = 0.507\,(1 - n)$. The remaining parameters, the mean velocity U, for the case without mass exchange, supplemented by the forward (k_f) and backward (k_r) mass exchange rates in the presence of mass exchange, are estimated by fitting the model of Equation 8 to the experimental breakthrough curves. The last two columns show the Reynolds $Re = \rho U\,d/\mu$ and the Peclet $Pe = U\,d/D_m$ numbers computed with the fitted mean velocity and for water density $\rho = 998.2$ kg/m^3 and viscosity $\mu = 1.002 \times 10^{-3}$ kg/(m s), both evaluated at 20°C.

or biomedical applications, or field-scale treatments such as In Situ Chemical Oxidation (Di Dato et al., 2018; Trefry et al., 2011, 2012; Wright et al., 2017). In particular, the fact that three of the nine subplanes contribute minimally to transport, while approximately 70% of the total mass arrives through just three quadrants, as highlighted in the inset of Figure 5, shows the impact of mesoscale heterogeneity and exchange processes, despite the porous media being constructed using hydrogel spheres of uniform size. The clusters of long accumulation times at the 95th percentile in Figures 4c and 4f mostly coincide with regions that accumulate only small amounts of mass (Figures 5a and 5b). Consequently, these long accumulation times exert a marginal influence on the BTC tails. This is further evidenced in the video of the Movie S1, which provides visual evidence that accumulation occurs far from the area potentially affected by tapering.

Figures 6a and 6b present the best fits of Equation 8 to the global experimental BTC (open symbols), considering mass exchange and neglecting mass exchange, respectively. In Equation 8, the expression (Equation 9) is replaced by its counterpart expression (Equation 20) when mass exchange is included. The fitted parameters are the mean velocity U for the purely hydrodynamic model, supplemented by the two exchange rates k_f and k_r, when mass exchange is considered. The remaining parameters are set to their experimentally measured values shown in Table 1. The fitting was performed using both the classical Fickian and the stochastic dispersivity models, leading respectively to the expressions (Equations 10 and A3) for the longitudinal residual displacement variance X_{11}. Notice that the dispersion parameters, namely α_L^{an} for the Fickian model, and λ and σ_Y^2 for the stochastic model, depend only on the diameter d and the porosity n, which are set to the experimental values shown in Table 1 and are not fitted. The fitted parameters are shown in Table 2.

Both experimental BTCs show long tails. Traditionally, such tailing has been attributed to a variety of processes, including homogeneous (Selroos & Cvetkovic, 1992) and spatially variable sorption (Bellin et al., 1993; Bellin & Rinaldo, 1995; Dentz & Castro, 2009), dual porosity (de Vries et al., 2017; Gerke & Van Genuchten, 1993; Leij et al., 2012), and mass exchange between mobile and immobile zones (e.g., Berkowitz et al., 2006; Park & Ji, 2018). While most of these processes leading to anomalous dispersion have been described at the field scale, laboratory-scale studies have also observed solute mass exchange due to the presence of stagnation zones and pore-scale diffusion-mediated transfer between fast and slow flow regions (Berkowitz et al., 2000, 2006). These effects are evident in Figures 4 and 5, as well as in the video of the Movie S1, and they contribute to more pronounced tailing than would occur under uniform advection and diffusion transport (Dentz et al., 2018; Haggerty & Gorelick, 1995). Moreover, the video shows that the channels forming within the porous medium, along which the solute moves, have an irregular geometry leading to a spatially variable velocity field. Also, we

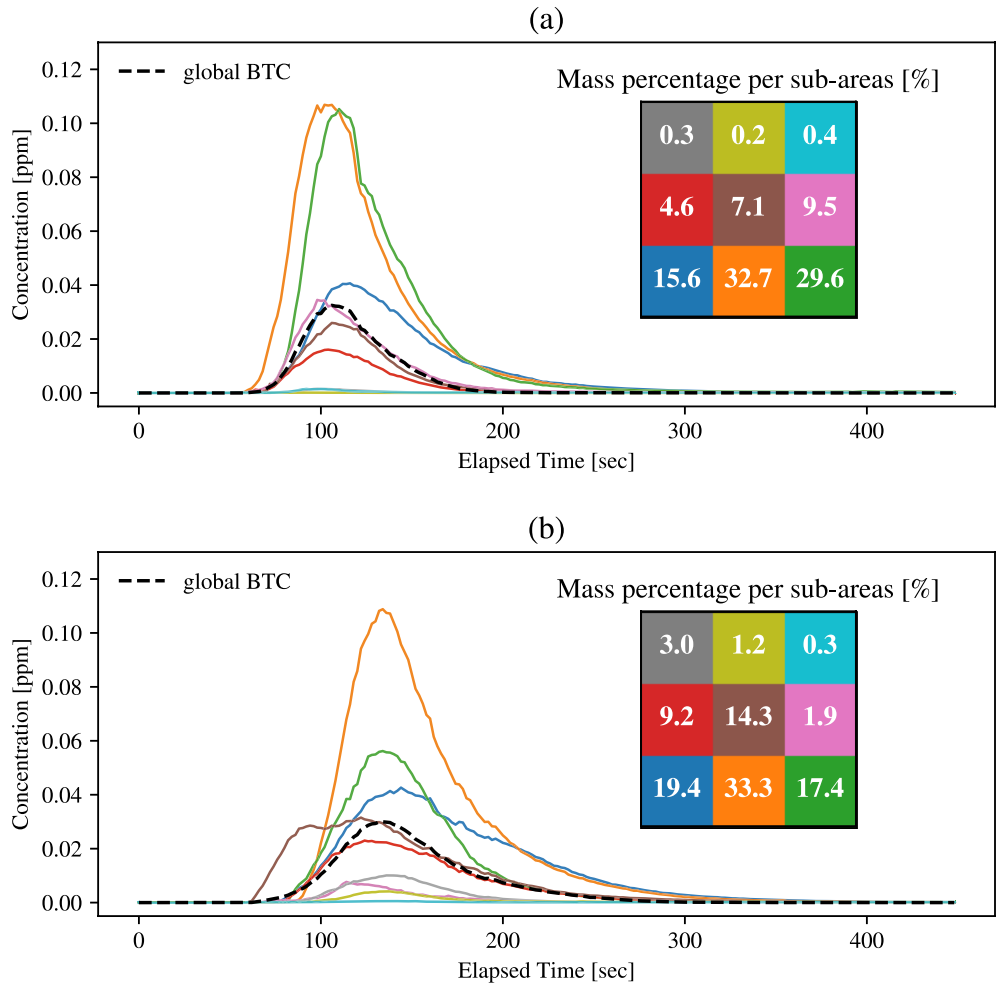

Figure 5. Local experimental breakthrough curves (BTCs) measured in nine equally sized subareas partitioning the control plane at $x_1 = 0.104$ m with a 3×3 grid (color-coded solid lines). The dashed black line shows the global BTC, evaluated over the entire control plane. The insets indicate the percentage of total mass passing through each subarea. Subarea colors correspond to the BTCs shown in the graph.

have verified that Rhodamine B behaves as a conservative tracer on hydrogel spheres within the time scale of our experiments, as described in Supporting Information S1.

Figures 6a and 6b show that both dispersion models successfully capture the full BTC, including its long tail, with negligible differences between them. Conversely, excluding mass exchange leads to narrower BTCs, due to reduced dispersivity in both the Fickian and stochastic models. This reflects the inability of models without mass exchange to account for the solute retention and delayed transport observed experimentally (see the video in Movie S1). This is further supported by the scatter plots in Figures 7a–7d, which show the modeled versus the experimental BTCs. These plots evidence that incorporating mass exchange significantly enhances the model's ability to predict the full BTC, particularly the late-time tailing (darker points), which is strongly influenced by slow transport processes associated with solute retention, i.e., transient storage.

Without mass exchange, transport is governed solely by advection and dispersion. With the Fickian model (blue lines in Figures 8a and 8b), dispersivity remains constant and X_{11} increases linearly with time. On the other hand, the stochastic model of X_{11}, given by Equation A3, results in a time-dependent dispersivity at early times (Equation A4) that asymptotically approaches a constant Fickian value. However, the pre-Fickian regime is very short, and this justifies the small differences observed between the Fickian and stochastic models in Figures 6a and 6b, and in Figures 7a–7d.

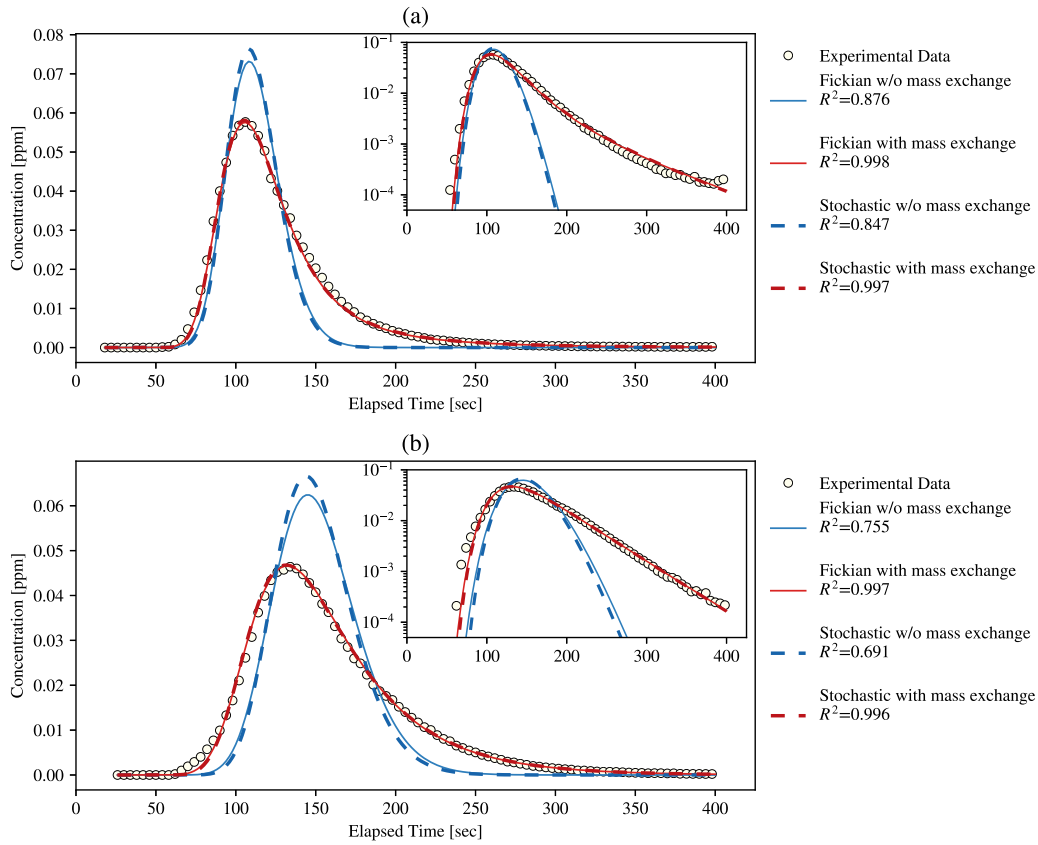

Figure 6. Experimental (open circles) and modeled breakthrough curves (BTCs) at the control plane $x_1 = 0.104$ m for (a) 10 mm and (b) 15 mm hydrogel spheres. Solid and dashed lines represent the BTC model given by Equation 8 using the Fickian (Equation 10 for the longitudinal second moment and 11 for the dispersivity) and stochastic (Equation A3 for the longitudinal second moment and Equation A4 for the dispersivity) dispersivity models, respectively. In the Fickian model we set the dispersivity α_L according to Equation 11, while in the stochastic model we set $\lambda = 3\,d/8$ and $\sigma_Y^2 = 8\,\alpha_L^{\mathrm{an}}/(3\,d) = 0.507\,(1 - n)$. Red and blue lines correspond to simulations with and without mass exchange, respectively.

Conversely, when mass exchange is included (red lines), dispersivity initially increases similarly to the case without mass exchange. However, it soon diverges from the constant Fickian value observed in the latter, first increasing linearly with time, and then at a sublinear rate. Therefore, the particle displacement variance X_{11}^{tr} grows more than linearly with time, as a consequence of a dispersivity that grows with time. The growth of dispersivity α_L highlights the non-Fickian nature of the transport, with mass exchange that controls tailing. Although strictly speaking, transport with mass exchange can be classified as non-Fickian, since α_L is time-dependent, we retain the commonly-used term anomalous transport to remark that its effects are most evident in the BTC tails.

4. Discussion

The BTC model (Equation 8) reproduces the experimental data accurately when dispersivity is set to the analytical expression α_L^{an} (Equation 11), and mass exchange is included. This result extends the applicability of the analytical expression (Equation 11), obtained under the diluted assumption, to a porous medium made of densely packed spheres with porosity of the order of $n = 0.3$.

The diluted approximation was shown to be applicable beyond its formal range in other cases, such as in computing the effective thermal properties (Jeffrey, 1973; Sangani & Acrivos, 1983) and the effective hydraulic conductivity (Jankovic et al., 2003) in highly heterogeneous porous media. The self-consistent approach was applied by Dagan and Fiori (2003) and Fiori and Dagan (2003) under the diluted assumption to simulate flow and transport in highly heterogeneous formations. With this model, Fiori et al. (2006, 2007) showed that the BTC tailing becomes more pronounced with increasing heterogeneity, due to the late arrival of the solute that is temporarily trapped in low-conductivity inclusions. These delayed arrivals extend the BTC tail relative to the bulk

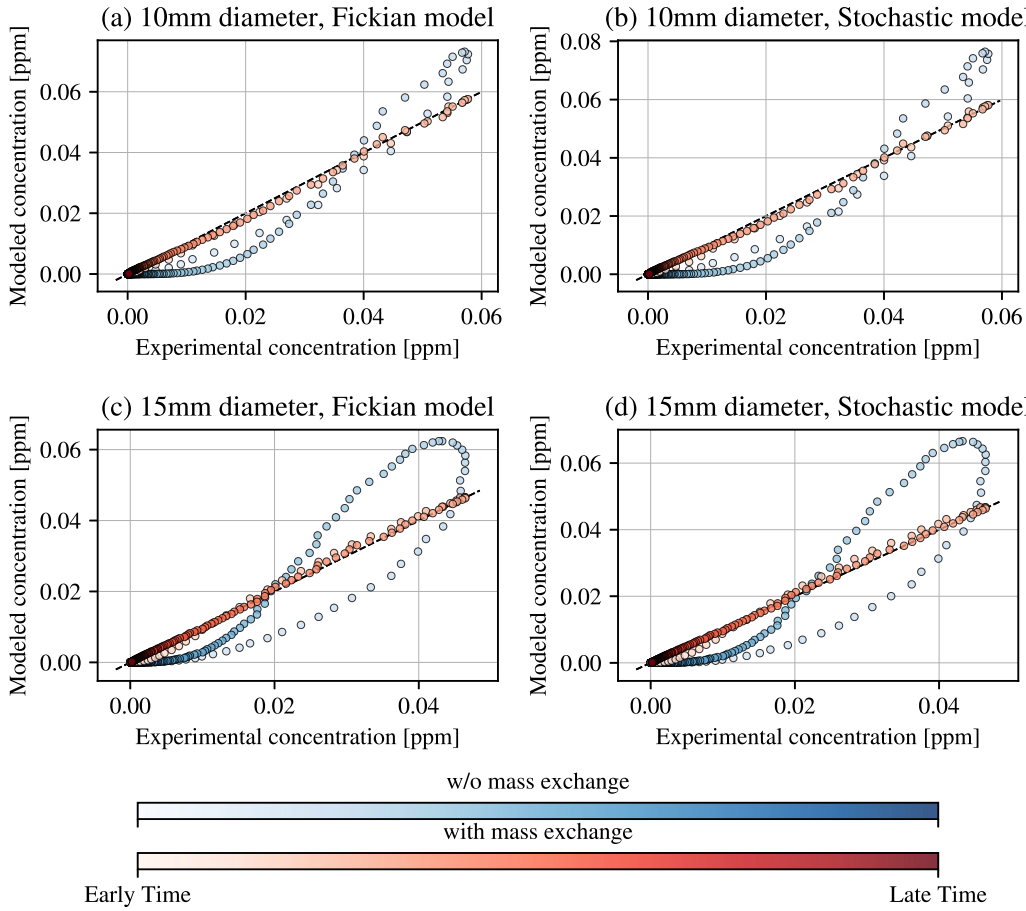

Figure 7. Scatter plots of the four models for hydrogel spheres of diameter (a, b) 10 mm and (c, d) 15 mm. Red colormaps represent cases with mass exchange, while blue indicates those without. To visualize how the agreement varies over time, the marker color darkens progressively as time increases.

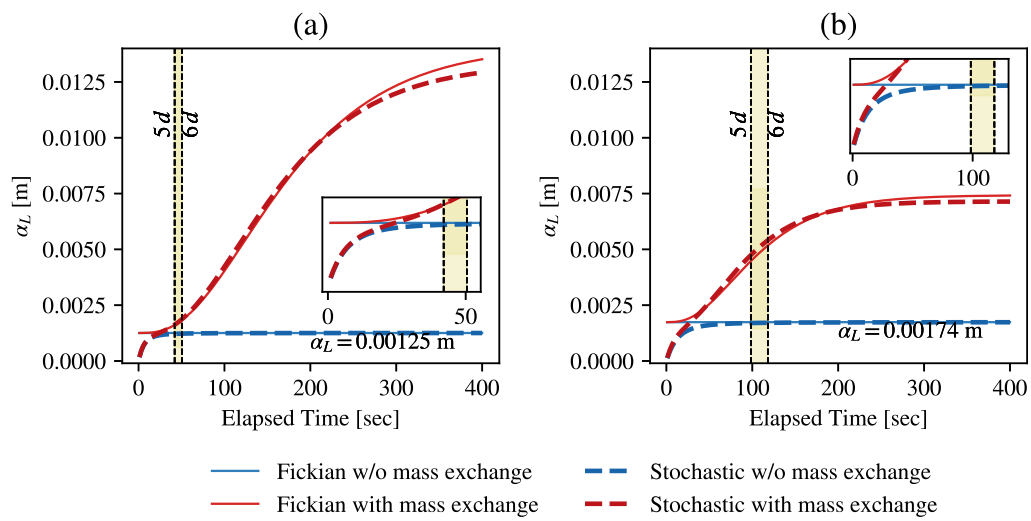

Figure 8. Longitudinal dispersivity α_L for (a) 10 mm and (b) 15 mm hydrogel spheres. Red and blue lines represent the cases with and without mass exchange, respectively. Insets show a zoomed view of the early time behavior. Vertical dashed lines indicate the times required to travel 5 and 6 sphere diameters (d), which Cushman and Moroni (2001) and Moroni and Cushman (2001a) suggested as the approximate time scale to reach Fickian behavior in their experiments.

of the solute plume. In our experiments, analogous mass exchange (a transient storage process) effects arise due to dead-end and low-velocity zones formed by the dense, random packing of the hydrogel spheres. Several authors observed experimentally the presence of such zones in a porous medium formed by spheres (Holzner et al., 2015; Rubol et al., 2018; Sanquer et al., 2024; Souzy et al., 2020), and De Anna et al. (2017) through accurate pore-scale numerical simulations. However, the high dilution hypothesis leads to a continuous velocity field in pore space without dead-end zones (see, Eames & Bush, 1999). As a consequence, the diluted model is unable to capture the tail of the experimental BTC. In contrast, when mass exchange is introduced via the classical mobile-immobile mass exchange model, the tailing is successfully reproduced. Although an additional delay may be induced by the recirculation zones that develop near the flow inlet, we believe this effect is localized and negligible compared to the global heterogeneity of the porous medium. This hypothesis is confirmed by the video of Movie S1, which shows how the tracer moves along a vertical plane crossing the central portion of the sample. We observe the appearance of dead-end and slow-moving zones at the contact of the spheres. Moreover, the fitted mean velocity is close to that estimated as the ratio between the specific discharge and porosity (see Tables 1 and 2), with the former obtained as the ratio between the volumetric flux and the cross-sectional area as described in Section 2.1.

When mass exchange is excluded, and the model (Equation 8) is fitted to the experimental data, the only fitting parameter is the mean velocity, which increases slightly with respect to that obtained including mass exchange. While a larger velocity leads to a higher hydrodynamic dispersion and a wider BTC, it causes a mismatch between the positions of the observed and computed peak concentrations, which acts as a strong limiting factor for the increase of the fitted mean velocity. The effect is that of computed BTCs remarkably narrower than the experimental ones, and with the peaks not perfectly aligned. The narrower BTCs result in a higher peak concentration, given that the mass should be conserved.

This finding highlights the limitations of the classical ADE to describe the observed transport behavior at the mesoscale, where the velocity field cannot be reproduced with accuracy down to the pore scale. A similar behavior was observed at the field scale, where macrodispersivity in the ADE should be reduced in proportion to the increase of the variability in the velocity field that the flow model is able to reproduce (see e.g., De Barros & Rubin, 2011; Rubin et al., 1999, 2003).

In environmental modeling, where data scarcity is common, there has been a preference for simpler models with fewer parameters to avoid equifinality, that is, a condition in which different parameter sets produce similar fits to the observed data (Beven, 2006). However, as discussed by Beven (2002), models should include all key processes governing the system behavior. In this context, the uncertainty arising from insufficient data to constrain disordered systems is better addressed by using stochastic methods, rather than oversimplifying the model, with the risk of omitting important processes (Rubin et al., 2018). Our findings support this view. Including mobile-immobile solute mass exchange is necessary to reproduce the BTC tails, despite increasing the number of fitted parameters from one to three. This process effectively mimics transient storage not captured by the smooth velocity field obtained under the diluted medium assumption. Importantly, because the BTC tail shape is primarily governed by the exchange parameters k_f and k_r, while the bulk of the BTC is controlled by advection and dispersion, the model is well-constrained, and all parameters can be accurately identified. Consequently our model does not suffer from equifinality. Despite the bulk of the BTC carrying much of the information needed to assess transport of passive solutes, the presence and shape of the tail can serve as an indicator of pore-scale mixing, a process relevant in the transport of reactive solutes.

The stochastic dispersivity model (Equation 12) we adopted in the present work was developed by Dagan (1984) for modeling macrodispersion at the field scale, and we showed here that it also applies at the mesoscale with the log-conductivity integral scale equal to $\lambda = 3\,d/8$. Figure 8 shows that the pre-asymptotic behavior is very short and the dispersivity converges quickly to the asymptotic first-order Fickian value $\alpha_L = 0.19\,d\,(1 - n)$ (see Equation 11). This explains why the Fickian and the stochastic models provide BTCs that are indistinguishable.

The characteristics of the velocity field and the behavior of the particle residual displacement X_{11} have been experimentally investigated in an early study by Cenedese and Viotti (1996) and later by Moroni and Cushman (2001b) in a porous medium composed of spherical Pyrex beads saturated with glycerol, and using air bubbles as a tracer. The former study proposed a two-dimensional analysis of the velocity field and the residual displacement variance, while the latter extended the analysis to three dimensions. A key result of this series of experimental investigations and theoretical developments (Cushman & Moroni, 2001; Moroni & Cushman, 2001a)

was that longitudinal dispersivity reaches the Fickian limit after a mean traveling distance of $5 \div 6\, d$. In our experiments, this distance is traveled in 42.0 ÷ 50.4 s and 98.4 ÷ 118.1 s for $d = 10$ and 15 mm, respectively, when the mean velocity is considered. At these times, the dispersivity provided by the FOA expression (Equation A4) reaches 96.7% ÷ 97.6% and 97.4% ÷ 98.1% of the asymptotic value (Equation 13) for $d = 10$ and 15 mm, respectively (see yellow vertical areas in Figures 8a and 8b). This agreement provides strong indirect validation, given the geometrical similarity of our experimental setup to those of Cenedese and Viotti (1996) and Moroni and Cushman (2001b), that our BTC model (Equation 8) accurately reproduces solute transport behavior at the mesoscale. In addition, since the transition to Fickian behavior occurs rapidly, dispersivity can be confidently set to the analytical value $\alpha_L = 0.19\, d(1 - n)$, with tailing chiefly controlled by the mass exchange parameters k_f and k_r.

The exchange process is characterized by relatively low forward k_f and backward k_r exchange rates, with partition coefficients $K_d = k_f/k_r$ of 0.291 and 0.252 for $d = 10$ and 15 mm, respectively, when the stochastic dispersivity model is used. For the Fickian model, these values are similar: 0.292 for $d = 10$ mm and 0.234 for $d = 15$ mm. The Dämkholer number, $Da = k_r \lambda / U$, provides the relative timescales of mass exchange and advection. Its value is equal to 0.042, for $d = 10$ mm, and 0.134, for $d = 15$ mm, for the stochastic dispersivity model using the asymptotic dispersivity α_L^{an} (see Equation 11 and Table 2). And similar values are obtained for the other cases. These low values indicate that the exchange process is slow relative to advection, that is, it is characterized by a long exchange time, and is thus exchange-limited. Exchange-limited transport suggests that only a relatively small amount of solute becomes temporarily trapped in the low velocity and stagnant zones, as indicated by the relatively low values of K_d for both the hydrogel bead diameters. According to Equation 16 the mass of solute per unit volume that temporarily accumulates in the immobile region obeys to the following (forward) exchange equation: $\partial C_{im}/\partial t = a_s J$, where $a_s = 6(1 - n)/d$ is the specific surface (exchange) area and J is the mass flux per unit area, which can be written as $J = k(C - C_{im})$, thereby leading to the following relationship $k_f = a_s k$ between k_f [T^{-1}] and the mass exchange rate k [L/T]. In an experimental study conducted with the $T_2 - T_2$ relaxation exchange NMR technique applied to packed beds formed by a random assemblage of TiO_2 spheres with a diameter of 3.1 mm Elgersma et al. (2022) obtained $k = (1.7 \pm 0.4)10^{-5}$ m/s for $Re = 10.1$ (see Table 2 of Elgersma et al. (2022)). Although TiO_2 is a sorbing material, its large grain diameter results in a relatively small sorption capacity in the packed bed, making it compatible with our porous medium, which is not affected by sorption. Using this value as a reference, in our case we obtain $k_f = (6.73 \pm 1.6) \times 10^{-3}$ s^{-1} and $(4.5 \pm 0.98) \times 10^{-3}$ s^{-1}, for $d = 10$ mm and 15 mm, respectively. These values are in good agreement with the fitted k_f values reported in Table 2, considering that, unlike hydrogel spheres, the TiO_2 grains possess sorption capacity. These differences notwithstanding, we conclude that our results are consistent with those obtained by Elgersma et al. (2022) using $T_2 - T_2$ relaxation exchange NMR.

The combination of small K_d and Da values is consistent with the interpretation that the long BTC tail is caused by the late arrival of a small amount of solute delayed in the low velocity zones, not captured by the simplified velocity field underlying the analytical dispersivity expression. In our model, this delay is effectively represented by a mobile-immobile mass exchange process. On the other hand, mass exchange exerts a negligible impact on the bulk BTC, as the majority of the solute is transported by advection and dispersion, with only a small amount of solute participating in the slow exchange process. The higher Da number for $d = 15$ mm evidences a relatively smaller impact of mass exchange compared to the $d = 10$ mm case. Although the analysis performed with only two diameters is not sufficient to draw general conclusions on how the exchange process depends on pore topology, we notice that larger bead diameters lead to larger pores and likely a smaller occurrence of low velocity, and stagnation zones, leading to a shorter delay of solute and a less persistent tail. As discussed previously, low velocity and stagnation zones at scales smaller than the REV have been experimentally evidenced by Rubol et al. (2018), in laboratory experiments conducted with hydrogel grains of irregular shapes, and in two-dimensional pore-scale simulations by De Anna et al. (2017).

5. Conclusions

The analysis of the BTC at a control plane in mesoscale transport experiments through porous media composed of hydrogel beads with uniform diameter revealed evidence of anomalous dispersion. This behavior results from the delayed arrival of a small amount of solute mass due to low velocity and stagnation zones that develop at the sub-REV scales. Although the porous medium is composed of spheres of uniform diameter, random packing generates heterogeneity in the distribution of voids. This likely gives rise to hydraulically preferential flow paths

interspersed with slow-flow and stagnant zones, promoting solute entrapment and the formation of transient storage zones that delay the propagation of solute.

To capture this complexity, we developed a solute transport model that combines advection and hydrodynamic pore-scale dispersion with mobile-immobile mass exchange, accounting for unresolved slow-flow and stagnant zones (transient storage). Fickian dispersivity is set according to the analytical expression of Equation 11, which depends only on the medium porosity and grain diameter. This model was developed by Eames and Bush (1999) under the highly diluted medium assumption (i.e., beads are far away from one another, leading to a porosity $n \rightarrow 1$). In addition, we considered two dispersivity models. The first one is the classic Fickian model with constant dispersivity given by Equation 11, and the second one is the pre-Fickian stochastic dispersion model developed by Dagan (1984) with a time-varying dispersivity converging to the same Fickian limit at times much larger than the characteristic advection time. When mass exchange is included, Fickian dispersivity is set according to the analytical expression (Equation 11), and the fitting parameters are the mean velocity U and the two exchange rates k_f and k_r. With this model, the experimental BTCs obtained with spheres of diameter $d = 10$ mm and 15 mm are accurately reproduced with a fitted mean velocity that is close to the one estimated experimentally (see Figures 6a and 6b). On the other hand, when mass exchange is not included, and only U is fitted, the model is unable to capture the tailing, and the dispersivity alone is not enough to capture the second-order moment of trajectories, which controls the contaminant dispersive behavior. However, the fitted mean velocity does not change appreciably with respect to the previous case, indicating that the parameters of our model are highly identifiable.

Overall, our results indicate that solute transport at the mesoscale is controlled by heterogeneity, even in visually uniform media, due to internal pore-scale variability, and the presence of zones of low and stagnant flow. The observed deviation from the classical Fickian behavior is not due to limitations of the Advection-Dispersion Equation itself, but rather to the inability of the flow model to accurately reproduce low-flow and stagnant zones, where transient storage and mass exchange occur. When these processes are included, through a mobile-immobile mass exchange model, the experimental BTCs are well reproduced. These results emphasize the importance of explicitly incorporating such mechanisms when modeling transport in porous media at the mesoscale.

The two dispersivity models show that at this scale, hydrodynamic dispersion reaches its Fickian limit at early times, when the solute has traveled only a few sphere diameters, and that the non-Fickian anomalous behavior can be reproduced by adding mass exchange between mobile and immobile zones. In addition, dispersivity and mass exchange process parameters are highly identifiable from the experimental BTCs because their effect can be easily separated; the former influences the bulk of the BTC, while the latter influences the tail.

Given that Rhodamine B behaves as a conservative tracer over the experimental timescale, the adopted mass-exchange model can effectively describe solute retention and the observed BTC tailing. In this framework, the fitted exchange parameters k_f and k_r represent the combined influence of transient storage and diffusive mass exchange arising from pore-scale heterogeneity, but can mimic the effects of other mechanisms, or in-homogeneities, causing retardation of the traveling plume.

Appendix A: Dispersivity Models

A1. Eames and Bush Inclusion Model

We consider the model of longitudinal dispersivity derived by Eames and Bush (1999) for porous media composed of inclusions of ellipsoidal impervious bodies into a uniform flow field. Assuming that the velocity between adjacent bodies decays exponentially with their reciprocal distance, the interaction between neighboring bodies vanishes as they are moved apart, making the media diluted and with high porosity. Under this condition, the hydrodynamic dispersion coefficient is given by half the time derivative of the second spatial moment of a line initially transverse to the mean velocity, that is deformed by the superimposition of the drifts generated by the inclusions. The dispersivity is then obtained by dividing the dispersion coefficient by the mean velocity:

$$\alpha_L^{an} = (1-n)\frac{2\mathcal{C}a^3}{b(b+a)}\left(\frac{a}{b}\cos^2\theta + \frac{b}{a}\sin^2\theta\right)^2 \tag{A1}$$

where a and b are the two ellipsoid radii, θ is the ellipsoid angle with respect to the mean flow direction, and C is the length-scale that characterizes the distortion of the inclusions' surface, which depends on the shape of the body. For spherical bodies $C = 0.38$ (Eames & Bush, 1999), which, substituted in Equation A1 together with $a = b = d/2$ and $\theta = 0$, leads to the expression (Equation 11).

A2. Stochastic First-Order Dispersivity Model

We consider here the stochastic model of macrodispersivity proposed by Dagan (1984, 1987) under the first order approximation of the Lagrangian velocity covariance function

$$v_{11}(t) \simeq u_{11}(tU/\lambda, 0, 0) = \frac{U^2}{(2\pi)^{3/2}} \iiint_{-\infty}^{\infty} dk_1\, dk_2\, dk_3 \left(1 - \frac{k_1^2}{k^2}\right)^2 \hat{C}_Y(\mathbf{k}) \exp(ik_1 t\, U/L) \tag{A2}$$

of a heterogeneous velocity field developing in a porous medium with the logconductivity $Y = \ln K$ - where K is the hydraulic conductivity - represented as a Normally distributed Random Space Function (RSF) with the following exponential isotropic log-conductivity covariance function $C_Y(\mathbf{r}) = \sigma_Y^2 \exp[-r/\lambda]$, which Fourier Transform is: $\hat{C}_Y(\mathbf{k}) = \frac{\lambda^3 \sigma_Y^2}{2\sqrt{2}} \exp[-\lambda^2 k^2/4]$. Here, r is the two-point separation distance, λ is the integral scale of Y, and $\mathbf{k} = (k_1, k_2, k_3)$ are the wave numbers. In Equation A2, the effect of molecular diffusion on the particle residual displacement variance is assumed negligible, given that in our experiments the Peclet number $Pe = U\lambda/D_m$ is larger than 1,000 for both 10 and 15 mm hydrogel spheres. The effect of diffusion in the longitudinal macrodispersion coefficient $D_{11} = 0.5\, d X_{11}/dt$ and therefore on X_{11} was, in fact, shown to be negligible for $Pe > 1000$ (Fiori, 1996; Figure 2).

By replacing Equation A2 into Equation 12. Dagan (1984) obtained the following first-order expression (in σ_Y^2) of the longitudinal second order moment:

$$X_{11}(t) = 2\lambda^2 \sigma_Y^2 \left\{ t' - \left[\frac{8}{3} - \frac{4}{t'} + \frac{8}{t'^3} - \frac{8}{t'^2}\left(1 + \frac{1}{t'}\right) e^{-t'} \right] \right\} + 2 D_m t, \quad t' = \frac{tU}{\lambda} \tag{A3}$$

Therefore, longitudinal dispersivity is given by

$$\alpha_L^{dag}(t) = \lambda \sigma_Y^2 \frac{e^{-t'} \left[e^{t'} \left(24 - 4t' + t'^4\right) - 8\left(3 + 3t' + t'^2\right) \right]}{t'^4} \tag{A4}$$

Acknowledgments
We thank Giorgia Giovannini of the Laboratory of Nanobiology and Nanotoxicology, Department of Biochemistry and Molecular Pharmacology, Istituto di Ricerche Farmacologiche Mario Negri IRCCS Milano (Italy), for the laboratory analysis of the Rhodamine B solutions sampled during the batch experiment. We are also grateful to the two anonymous reviewers for the insightful and constructive comments. Alberto Bellin and Mariaines di Dato acknowledge funding by the PNRR project iNEST (Interconnected NordEst Innovation Ecosystem), Mission 4.2, Investment 1.5, NextGeneration EU (Project ID: ECS 00000043, Digital, Industry, Aerospace). Prasanjaya Ekanayake and Alberto Bellin acknowledge the support by the project DICAM-EXC (Departments of Excellence 2023–2027, Grant L232/2016), funded by the Italian Ministry of University and Research (MUR). Daniele Tonina was partially supported by Hatch Act (Accession Number IDA01722) through the USDA National Institute of Food and Agriculture. Open access publishing facilitated by Università degli Studi di Trento, as part of the Wiley - CRUI-CARE agreement.

Conflict of Interest

The authors declare no conflicts of interest relevant to this study.

Data Availability Statement

The Python Notebook used to build the models is available under the MIT license and published on Zenodo (Di Dato et al., 2025, https://doi.org/10.5281/zenodo.15553717) together with the experimental data produced for the analysis. Figures were made with Matplotlib version 3.2.1 Caswell et al. (2020); Hunter (2007), available under the Matplotlib license at https://matplotlib.org/.

References

Alves, J. R., Berg, L. A., Gaio, E. D., Rocha, B. M., De Queiroz, R. A. B., & Dos Santos, R. W. (2023). A hybrid model for cardiac perfusion: Coupling a discrete coronary arterial tree model with a continuous porous-media flow model of the myocardium. *Entropy*, *25*(8), 1229. https://doi.org/10.3390/e25081229

Basham, W., Budwig, R., & Tonina, D. (2019). Particle seeded grains to identify highly irregular solid boundaries and simplify PIV measurements. *Frontiers in Earth Science*, *7*, 195. https://doi.org/10.3389/feart.2019.00195

Basilio Hazas, M., Ziliotto, F., Rolle, M., & Chiogna, G. (2022). Linking mixing and flow topology in porous media: An experimental proof. *Physical Review E - Statistical Physics, Plasmas, Fluids, and Related Interdisciplinary Topics*, *105*(3), 035105. https://doi.org/10.1103/PhysRevE.105.035105

Bear, J. (1972). *Dynamics of fluids in porous media*. Elsevier.

Bellin, A., & Rinaldo, A. (1995). Analytical solutions for transport of linearly adsorbing solutes in heterogeneous formations. *Water Resources Research*, *31*(6), 1505–1511. https://doi.org/10.1029/95WR00200

Bellin, A., Rinaldo, A., Bosma, W. J. P., van der Zee, S. E. A. T. M., & Rubin, Y. (1993). Linear equilibrium adsorbing solute transport in physically and chemically heterogeneous porous formations: 1. Analytical solutions. *Water Resources Research*, *29*(12), 4019–4030. https://doi.org/10.1029/93WR02303

Berkowitz, B., Cortis, A., Dentz, M., & Scher, H. (2006). Modeling non-fickian transport in geological formations as a continuous time random walk. *Reviews of Geophysics*, *44*(2). https://doi.org/10.1029/2005RG000178

Berkowitz, B., & Scher, H. (2010). Anomalous transport in correlated velocity fields. *Physical Review E*, *81*(1), 011128. https://doi.org/10.1103/PhysRevE.81.011128

Berkowitz, B., Scher, H., & Silliman, S. E. (2000). Anomalous transport in laboratory-scale, heterogeneous porous media. *Water Resources Research*, *36*(1), 149–158. https://doi.org/10.1029/1999WR900295

Bertran, O., Fernàndez-Garcia, D., Sole-Mari, G., & Rodríguez-Escales, P. (2023). Enhancing mixing during groundwater remediation via engineered injection-extraction: The issue of connectivity. *Water Resources Research*, *59*(7), e2023WR034934. https://doi.org/10.1029/2023WR034934

Betancur, S., Quevedo, L., & Olmos, C. M. (2024). Microfluidic devices, materials, and recent progress for petroleum applications: A review. *Canadian Journal of Chemical Engineering*, *102*(7), 2583–2607. https://doi.org/10.1002/cjce.24877

Beven, K. (2002). Towards a coherent philosophy for modelling the environment. *Proceedings of the Royal Society of London. Series A: Mathematical, Physical and Engineering Sciences*, *458*(2026), 2465–2484. https://doi.org/10.1098/rspa.2002.0986

Beven, K. (2006). A manifesto for the equifinality thesis. *Journal of Hydrology*, *320*(1–2), 18–36. https://doi.org/10.1016/j.jhydrol.2005.07.007

Bhattacharjee, T., & Datta, S. S. (2019). Bacterial hopping and trapping in porous media. *Nature Communications*, *10*(1), 2075. https://doi.org/10.1038/s41467-019-10115-1

Budwig, R. (1994). Refractive index matching methods for liquid flow investigations. *Experiments in Fluids*, *17*(5), 350–355. https://doi.org/10.1007/bf01874416

Butler, S. L., Kohles, S. S., Thielke, R. J., Chen, C., & Vanderby, R. (1997). Interstitial fluid flow in tendons or ligaments: A porous medium finite element simulation. *Medical, & Biological Engineering & Computing*, *35*(6), 742–746. https://doi.org/10.1007/bf02510987

Caswell, T. A., Droettboom, M., Lee, A., Hunter, J., Firing, E., Stansby, D., et al. (2020). Matplotlib/matplotlib v3.2.1 [Software]. *Zenodo*. https://doi.org/10.5281/zenodo.3714460

Cenedese, A., & Viotti, P. (1996). Lagrangian analysis of nonreactive pollutant dispersion in porous media by means of the particle image velocimetry technique. *Water Resources Research*, *32*(8), 2329–2343. https://doi.org/10.1029/96WR00605

Chen, C. S., & Niklason, L. E. (2012). Engineering human blood vessels from pluripotent stem cells. *Journal of Clinical Investigation*, *122*(4), 1323–1328.

Coats, K., & Smith, B. (1964). Dead-end pore volume and dispersion in porous media. *Society of Petroleum Engineers Journal*, *4*(1), 73–84. https://doi.org/10.2118/647-PA

Cookson, A. N., Lee, J., Michler, C., Chabiniok, R., Hyde, E., Nordsletten, D. A., et al. (2012). A novel porous mechanical framework for modelling the interaction between coronary perfusion and myocardial mechanics. *Journal of Biomechanics*, *45*(5), 850–855. https://doi.org/10.1016/j.jbiomech.2011.11.026

Cushman, J. H., & Moroni, M. (2001). Statistical mechanics with three-dimensional particle tracking velocimetry experiments in the study of anomalous dispersion. I. Theory. *Physics of Fluids*, *13*(1), 75–80. https://doi.org/10.1063/1.1328075

Dagan, G. (1984). Solute transport in heterogeneous porous formations. *Journal of Fluid Mechanics*, *145*, 151–177. https://doi.org/10.1017/S0022112084002858

Dagan, G. (1987). Theory of solute transport by groundwater. *Annual Review of Fluid Mechanics*, *19*(1), 183–215. https://doi.org/10.1146/annurev.fl.19.010187.001151

Dagan, G. (1989). *Flow and transport in porous formations*. Springer-Verlag. https://doi.org/10.1007/978-3-642-75015-1

Dagan, G., & Fiori, A. (2003). Time-dependent transport in heterogeneous formations of bimodal structures: 1. the model. *Water Resources Research*, *39*(5). https://doi.org/10.1029/2002WR001396

Dantec Dynamics A/S. (2021). DynamicStudio User Manual. Dantec Dynamics A/S. Retrieved from https://www.dantecdynamics.com

Datta, S. S., Chiang, H., Ramakrishnan, T. S., & Weitz, D. A. (2013). Spatial fluctuations of fluid velocities in flow through a three-dimensional porous medium. *Physical Review Letters*, *111*(6), 064501. https://doi.org/10.1103/PhysRevLett.111.064501

Datta, S. S., Dupin, J.-B., & Weitz, D. A. (2014). Fluid breakup during simultaneous two-phase flow through a three-dimensional porous medium. *Physics of Fluids*, *26*(6), 062004. https://doi.org/10.1063/1.4884955

Datta, S. S., Ramakrishnan, T. S., & Weitz, D. A. (2014). Mobilization of a trapped non-wetting fluid from a three-dimensional porous medium. *Physics of Fluids*, *26*(2), 022002. https://doi.org/10.1063/1.4866641

Datta, S. S., & Weitz, D. A. (2013). Drainage in a model stratified porous medium. *Europhysics Letters*, *101*(1), 14002. https://doi.org/10.1209/0295-5075/101/14002

De Anna, P., Quaife, B., Biros, G., & Juanes, R. (2017). Prediction of the low-velocity distribution from the pore structure in simple porous media. *Physical Review Fluids*, *2*(12), 124103. https://doi.org/10.1103/PhysRevFluids.2.124103

De Barros, F. P. J., & Rubin, Y. (2011). Modelling of block-scale macrodispersion as a random function. *Journal of Fluid Mechanics*, *676*, 514–545. https://doi.org/10.1017/jfm.2011.65

Delgado, J. M. P. Q. (2006). A critical review of dispersion in packed beds. *Heat and Mass Transfer*, *42*(4), 279–310. https://doi.org/10.1007/s00231-005-0019-0

Dentz, M., & Castro, A. (2009). Effective transport dynamics in porous media with heterogeneous retardation properties. *Geophysical Research Letters*, *36*(3). https://doi.org/10.1029/2008GL036846

Dentz, M., Icardi, M., & Hidalgo, J. J. (2018). Mechanisms of dispersion in a porous medium. *Journal of Fluid Mechanics*, *841*, 851–882. https://doi.org/10.1017/jfm.2018.120

de Vries, E. T., Raoof, A., & van Genuchten, M. T. (2017). Multiscale modelling of dual-porosity porous media; a computational pore-scale study for flow and solute transport. *Advances in Water Resources*, *105*, 82–95. https://doi.org/10.1016/j.advwatres.2017.04.013

Di Dato, M., de Barros, F. P. J., Fiori, A., & Bellin, A. (2018). Improving the efficiency of 3-D hydrogeological mixers: Dilution enhancement via coupled engineering-induced transient flows and spatial heterogeneity. *Water Resources Research*, *54*(3), 2095–2111. https://doi.org/10.1002/2017WR022116

Di Dato, M., Ekanayake, P., & Bellin, A. (2025). Code and data for "capturing Non-Fickian mesoscale solute transport in porous media: The role of transient storage and mass exchange. [computational notebook, Dataset]. *Zenodo*. https://doi.org/10.5281/zenodo.15553717

Di Dato, M., Fiori, A., Chiogna, G., de Barros, F. P. J., & Bellin, A. (2016). Impact of the spatial structure of the hydraulic conductivity field on vorticity in three-dimensional flows. *Proceedings of the Royal Society A: Mathematical, Physical and Engineering Sciences*, *472*(2187), 20150730. https://doi.org/10.1098/rspa.2015.0730

Dyson, P., Ransing, R., Williams, P. H., & Williams, R. (2008). *Fluid properties at nano/meso scale: A numerical treatment*. John Wiley & Sons.

Eames, I., & Bush, J. W. M. (1999). Longitudinal dispersion by bodies fixed in a potential flow. *Proceedings of the Royal Society of London*, *455*(1990), 3665–3686. https://doi.org/10.1098/rspa.1999.0471

Edery, Y., Dror, I., Scher, H., & Berkowitz, B. (2015). Anomalous reactive transport in porous media: Experiments and modeling. *Physical Review E*, *91*(5), 052130. https://doi.org/10.1103/physreve.91.052130

Elgersma, S. V., Sederman, A. J., Mantle, M. D., & Gladden, L. F. (2022). Measuring the liquid-solid mass transfer coefficient in packed beds using t2-t2 relaxation exchange NMR. *Chemical Engineering Science*, *248*, 117229. https://doi.org/10.1016/j.ces.2021.117229

Facchini, L., Bellin, A., & Toro, E. F. (2014). A mathematical model for filtration and macromolecule transport across capillary walls. *Microvascular Research*, *94*, 52–63. https://doi.org/10.1016/j.mvr.2014.05.001

Fathiganjehlou, A., Eghbalmanesh, A., Baltussen, M. W., Peters, E. A. J. F., Buist, K. A., & Kuipers, J. A. M. (2023). Pore network modelling of slender packed bed reactors. *Chemical Engineering Science*, *273*, 118626. https://doi.org/10.1016/j.ces.2023.118626

Fiori, A. (1996). Finite peclet extensions of Dagan's solutions to transport in anisotropic heterogeneous formations. *Water Resources Research*, *32*(1), 193–198. https://doi.org/10.1029/95WR02768

Fiori, A., Bellin, A., Cvetkovic, V., de Barros, F. P. J., & Dagan, G. (2015). Stochastic modeling of solute transport in aquifers: From heterogeneity characterization to risk analysis. *Water Resources Research*, *51*(8), 6622–6648. https://doi.org/10.1002/2015WR017388

Fiori, A., & Dagan, G. (2003). Time-dependent transport in heterogeneous formations of bimodal structures: 2. results. *Water Resources Research*, *39*(5). https://doi.org/10.1029/2002WR001398

Fiori, A., Janković, I., & Dagan, G. (2006). Modeling flow and transport in highly heterogeneous three-dimensional aquifers: Ergodicity, gaussianity, and anomalous behavior—2. approximate semianalytical solution. *Water Resources Research*, *42*(6). https://doi.org/10.1029/2005WR004752

Fiori, A., Janković, I., Dagan, G., & Cvetković, V. (2007). Ergodic transport through aquifers of non-gaussian log conductivity distribution and occurrence of anomalous behavior. *Water Resources Research*, *43*(9). https://doi.org/10.1029/2007WR005976

Foster, A., Trautz, A. C., Bolster, D., Illangasekare, T., & Singha, K. (2021). Effects of large-scale heterogeneity and temporally varying hydrologic processes on estimating immobile pore space: A mesoscale-laboratory experimental and numerical modeling investigation. *Journal of Contaminant Hydrology*, *241*, 103811. https://doi.org/10.1016/j.jconhyd.2021.103811

Gelhar, L. W. (1986). Stochastic subsurface hydrology from theory to application. *Water Resources Research*, *22*(suppl.), 135S–145S.

Gelhar, L. W. (1993). *Stochastic subsurface hydrology*. Prentice-Hall.

Gelhar, L. W., & Axness, C. L. (1983). Three-dimensional stochastic analysis of macrodispersion in aquifers. *Water Resources Research*, *19*(1), 161–180. https://doi.org/10.1029/wr019i001p00161

Gerke, H. H., & Van Genuchten, M. T. (1993). A dual-porosity model for simulating the preferential movement of water and solutes in structured porous media. *Water Resources Research*, *29*(2), 305–319. https://doi.org/10.1029/92wr02339

Haggerty, R., & Gorelick, S. M. (1995). Multiple-rate mass transfer for modeling diffusion and surface reactions in media with pore-scale heterogeneity. *Water Resources Research*, *31*(10), 2383–2400. https://doi.org/10.1029/95WR10583

Hilliard, B., Budwig, R., Skifton, R. S., Durgesh, V., Reeder, W. J., Bhattarai, B., et al. (2023). Measuring porous media velocity fields and grain bed architecture with a quantitative plif-based technique. *Measurement Science and Technology*, *34*(12), 125805. https://doi.org/10.1088/1361-6501/acfb2b

Holzner, M., Morales, V. L., Willmann, M., & Dentz, M. (2015). Intermittent lagrangian velocities and accelerations in three-dimensional porous medium flow. *Physical Review E - Statistical Physics, Plasmas, Fluids, and Related Interdisciplinary Topics*, *92*(1), 013015. https://doi.org/10.1103/PhysRevE.92.013015

Hu, Q., Yang, X., Huang, L., Li, Y., Hao, L., Pei, Q., & Pei, X. (2024). A critical review of breakthrough models with analytical solutions in a fixed-bed column. *Journal of Water Process Engineering*, *59*, 105065. https://doi.org/10.1016/j.jwpe.2024.105065

Huang, A. Y., Huang, M. Y., Capart, H., & Chen, R.-H. (2008). Optical measurements of pore geometry and fluid velocity in a bed of irregularly packed spheres. *Experiments in Fluids*, *45*(2), 309–321. https://doi.org/10.1007/s00348-008-0480-x

Hunter, J. D. (2007). Matplotlib: A 2D graphics environment. *Computing in Science & Engineering*, *9*(3), 90–95. https://doi.org/10.1109/MCSE.2007.55

Iraji, S., De Almeida, T. R., Munoz, E. R., Basso, M., & Vidal, A. C. (2024). The impact of heterogeneity and pore network characteristics on single and multi-phase fluid propagation in complex porous media: An x-ray computed tomography study. *Petroleum Science*.

Iskander, M., Bathurst, R. J., & Omidvar, M. (2015). Past, present, and future of transparent soils. *Geotechnical Testing Journal*, *38*(5), 557–573. https://doi.org/10.1520/GTJ20150079

Izaguirre, M., & Parsa, S. (2024). Emergence of preferential flow paths and intermittent dynamics in emulsion transport in porous media. *Soft Matter*, *20*(17), 3585–3592. https://doi.org/10.1039/D3SM01465G

Jankovic, I., Fiori, A., & Dagan, G. (2003). Effective conductivity of an isotropic heterogeneous medium of lognormal conductivity distribution. *Multiscale Modeling and Simulation*, *1*(1), 40–56. https://doi.org/10.1137/S1540345902409633

Jeffrey, D. J. (1973). Conduction through a random suspension of spheres. *Proceedings of the Royal Society of London. A. Mathematical and Physical Sciences*, *335*(1602), 355–367. https://doi.org/10.1098/rspa.1973.0130

Jia, G., Huang, H., Niu, J., Chen, C., Weng, J., Yu, F., et al. (2021). Exploring the interconnectivity of biomimetic hierarchical porous mg scaffolds for bone tissue engineering: Effects of pore size distribution on mechanical properties, degradation behavior and cell migration ability. *Journal of Magnesium and Alloys*, *9*(6), 1954–1966. https://doi.org/10.1016/j.jma.2021.02.001

Karimi, M., & Bhattya, K. (2024). Accelerated computational micromechanics for solute transport in porous media. *Computer Methods in Applied Mechanics and Engineering*, *426*, 116976. https://doi.org/10.1016/j.cma.2024.116976

Kasai, Y., Jinbo, Y., Kamikawa, H., & Sanada, T. (2024). Global and local breakthrough curves: A concept for filtration design through analysis of internal concentration distribution using CFD. *Chemical Engineering Research and Design*.

Keller, R. A., & Giddings, J. C. (1960). Multiple zones and spots in chromatography. *Journal of Chromatography A*, *3*, 205–220. https://doi.org/10.1016/s0021-9673(01)96983-3

Kennedy, C., & Lennox, W. (2001). A stochastic interpretation of the tailing effect in solute transport. *Stochastic Environmental Research and Risk Assessment*, *15*(4), 325–340. https://doi.org/10.1007/s004770100076

Kim, S., & Russel, W. B. (1985). Modelling of porous media by renormalization of the stokes equations. *Journal of Fluid Mechanics*, *154*, 269–286. https://doi.org/10.1017/S0022112085001525

Kim, S.-B., Jo, K.-H., Kim, D.-J., & Jury, W. A. (2004). Determination of two-dimensional laboratory-scale dispersivities. *Hydrological Processes*, *18*(13), 2475–2483. https://doi.org/10.1002/hyp.1475
Kitanidis, P. K. (1994). The concept of the dilution index. *Water Resources Research*, *30*(7), 2011–2026. https://doi.org/10.1029/94WR00762
Koch, D. L., & Brady, J. F. (1985). Dispersion in fixed beds. *Journal of Fluid Mechanics*, *154*, 399–427. https://doi.org/10.1017/S0022112085001598
Krol, Q., Fouxon, I., Corso, P., & Holzner, M. (2021). Local hydraulic resistance in heterogeneous porous media. *Geophysical Research Letters*, *48*(22), e2021GL094694. https://doi.org/10.1029/2021GL094694
Lachhab, A., Zhang, Y.-K., & Muste, M. V. (2008). Particle tracking experiments in match-index-refraction porous media. *Groundwater Series*, *46*(6), 865–872. https://doi.org/10.1111/j.1745-6584.2008.00479.x
Lan, D., Zhu, H., Zhang, J., Li, S., Chen, Q., Wang, C., et al. (2022). Adsorptive removal of organic dyes via porous materials for wastewater treatment in recent decades: A review on species, mechanisms and perspectives. *Chemosphere*, *293*, 133464. https://doi.org/10.1016/j.chemosphere.2021.133464
Lebon, L., Oger, L., Leblond, J., Hulin, J. P., Martys, N. S., & Schwartz, L. M. (1996). Pulsed gradient nmr measurements and numerical simulation of flow velocity distribution in sphere packings. *Physics of Fluids*, *8*(2), 293–301. https://doi.org/10.1063/1.868839
Leij, F. J., Toride, N., Field, M. S., & Sciortino, A. (2012). Solute transport in dual-permeability porous media. *Water Resources Research*, *48*(4). https://doi.org/10.1029/2011wr011502
Liu, Y., Xiao, H., Aquino, T., Dentz, M., & Wang, M. (2024). Scaling laws and mechanisms of hydrodynamic dispersion in porous media. *Journal of Fluid Mechanics*, *1001*, R2. https://doi.org/10.1017/jfm.2024.1131
MacMinn, C. W., Dufresne, E. R., & Wettlaufer, J. S. (2015). Fluid-driven deformation of a soft granular material. *Physical Review X*, *5*(1), 011020. https://doi.org/10.1103/PhysRevX.5.011020
MacMinn, C. W., Dufresne, E. R., & Wettlaufer, J. S. (2016). Large deformations of a soft porous material. *Physical Review Applied*, *5*(4), 044020. https://doi.org/10.1103/PhysRevApplied.5.044020
Magnico, P. (2003). Hydrodynamic and transport properties of packed beds in small tube-to-sphere diameter ratio: Pore scale simulation using an Eulerian and a lagrangian approach. *Chemical Engineering Science*, *58*(22), 5005–5024. https://doi.org/10.1016/S0009-2509(03)00282-3
Massabó, M., Bellin, A., & Valocchi, A. J. (2008). Spatial moments analysis of kinetically sorbing solutes in aquifer with bimodal permeability distribution. *Water Resources Research*, *44*(9). https://doi.org/10.1029/2007WR006539
Moradi, G., & Mehdinejadiani, B. (2020). An experimental study on scale dependency of fractional dispersion coefficient. *Arabian Journal of Geosciences*, *13*(11), 1–13. https://doi.org/10.1007/s12517-020-05438-z
Moroni, M., & Cushman, J. H. (2001a). Statistical mechanics with three-dimensional particle tracking velocimetry experiments in the study of anomalous dispersion. II. experiments. *Physics of Fluids*, *13*(1), 81–91. https://doi.org/10.1063/1.1328076
Moroni, M., & Cushman, J. H. (2001b). Three-dimensional particle tracking velocimetry studies of the transition from pore dispersion to fickian dispersion for homogeneous porous media. *Water Resources Research*, *37*(4), 873–884. https://doi.org/10.1029/2000WR900364
Moroni, M., Kleinfelter, N., & Cushman, J. H. (2007). Analysis of dispersion in porous media via matched-index particle tracking velocimetry experiments. *Advances in Water Resources*, *30*(1), 1–15. https://doi.org/10.1016/j.advwatres.2006.02.005
Naftaly, A., Edery, Y., Dror, I., & Berkowitz, B. (2015). Visualization and analysis of nanoparticle transport and ageing in reactive porous media. *Journal of Hazardous Materials*, *299*, 513–519. https://doi.org/10.1016/j.jhazmat.2015.07.043
Nissan, A., & Berkowitz, B. (2019). Anomalous transport dependence on péclet number, porous medium heterogeneity, and a temporally varying velocity field. *Physical Review E*, *99*(3), 033108. https://doi.org/10.1103/physreve.99.033108
Nissan, A., Dror, I., & Berkowitz, B. (2017a). Time-dependent velocity-field controls on anomalous chemical transport in porous media. *Water Resources Research*, *53*(5), 3760–3769. https://doi.org/10.1002/2016wr020143
Nissan, A., Dror, I., & Berkowitz, B. (2017b). Time-dependent velocity-field controls on anomalous chemical transport in porous media. *Water Resources Research*, *53*(5), 3760–3769. https://doi.org/10.1002/2016WR020143
Ou, Z., Xue, Q., Wan, Y., Wei, H., Liu, L., Gharibi, F., & Thévenin, D. (2024). A one-field fluid/meso-structure coupling approach for multiscale transport in heterogeneous porous media. *Physics of Fluids*, *36*(11), 113112. https://doi.org/10.1063/5.0239940
Pang, L., Goltz, M., & Close, M. (2003). Application of the method of temporal moments to interpret solute transport with sorption and degradation. *Journal of Contaminant Hydrology*, *60*(1), 123–134. https://doi.org/10.1016/S0169-7722(02)00061-X
Park, D. K., & Ji, S.-H. (2018). Numerical simulation of anomalous observations from an in-situ long-term sorption diffusion experiment in a rock matrix. *Journal of Hydrology*, *565*, 502–515. https://doi.org/10.1016/j.jhydrol.2018.08.058
Parsa, S., Santanach-Carreras, E., Xiao, L., & Weitz, D. A. (2020). Origin of anomalous polymer-induced fluid displacement in porous media. *Physical Review Fluids*, *5*(2), 022001. https://doi.org/10.1103/PhysRevFluids.5.022001
Parsa, S., Zareei, A., Santanach-Carreras, E., Morris, E. J., Amir, A., Xiao, L., & Weitz, D. A. (2021). Unexpected scaling of interstitial velocities with permeability due to polymer retention in porous media. *Physical Review Fluids*, *6*(8), L082302. https://doi.org/10.1103/PhysRevFluids.6.L082302
Peppas, N. A. (2000). Hydrogels in pharmaceutical formulations. *European Journal of Pharmaceutics and Biopharmaceutics*, *50*(1), 27–46. https://doi.org/10.1016/s0939-6411(00)00090-4
Porta, G. M., Bijeljic, B., Blunt, M. J., & Guadagnini, A. (2015). Continuum-scale characterization of solute transport based on pore-scale velocity distributions. *Geophysical Research Letters*, *42*(18), 7537–7545. https://doi.org/10.1002/2015GL065423
Puyguiraud, A., Gouze, P., & Dentz, M. (2021). Pore-scale mixing and the evolution of hydrodynamic dispersion in porous media. *Physical Review Letters*, *126*(16), 164501. https://doi.org/10.1103/PhysRevLett.126.164501
Quinodoz, H. A. M., & Valocchi, A. J. (1993). Stochastic analysis of the transport of kinetically sorbing solutes in aquifers with randomly heterogeneous hydraulic conductivity. *Water Resources Research*, *29*(9), 3227–3240. https://doi.org/10.1029/93WR01039
Rao, P. S. C., Rolston, D. E., Jessup, R. E., & Davidson, J. M. (1980). Solute transport in aggregated porous media: Theoretical and experimental evaluation. *Soil Science Society of America Journal*, *44*(6), 1139–1146. https://doi.org/10.2136/sssaj1980.03615995004400060003x
Rashidi, M., Peurrung, L., Tompson, A. F. B., & Kulp, T. J. (1996). Experimental analysis of pore-scale flow and transport in porous media. *Advances in Water Resources*, *19*(3), 163–180. https://doi.org/10.1016/0309-1708(95)00048-8
Rau, G. C., Andersen, M. S., & Acworth, R. I. (2012). Experimental investigation of the thermal dispersivity term and its significance in the heat transport equation for flow in sediments. *Water Resources Research*, *48*(3), W03511. https://doi.org/10.1029/2011wr011038
Rolle, M., & Kitanidis, P. K. (2014). Effects of compound-specific dilution on transient transport and solute breakthrough: A pore-scale analysis. *Advances in Water Resources*, *71*, 186–199. https://doi.org/10.1016/j.advwatres.2014.06.012
Rubin, Y. (2003). *Applied stochastic hydrogeology*. Oxford University Press. https://doi.org/10.1093/oso/9780195138047.001.0001
Rubin, Y., Bellin, A., & Lawrence, A. E. (2003). On the use of block-effective macrodispersion for numerical simulations of transport in heterogeneous formations. *Water Resources Research*, *39*(9). https://doi.org/10.1029/2002WR001727

Rubin, Y., Chang, C.-F., Chen, J., Cucchi, K., Harken, B., Heße, F., & Savoy, H. (2018). Stochastic hydrogeology's biggest hurdles analyzed and its big blind spot. *Hydrology and Earth System Sciences*, *22*(11), 5675–5695. https://doi.org/10.5194/hess-22-5675-2018

Rubin, Y., Sun, A., Maxwell, R., & Bellin, A. (1999). The concept of block-effective macrodispersivity and a unified approach for grid-scale- and plume-scale-dependent transport. *Journal of Fluid Mechanics*, *395*, 161–180. https://doi.org/10.1017/S0022112099005868

Rubol, S., Tonina, D., Vincent, L., Sohm, J. A., Basham, W., Budwig, R., et al. (2018). Seeing through porous media: An experimental study for unveiling interstitial flows. *Hydrological Processes*, *32*(3), 402–407. https://doi.org/10.1002/hyp.11425

Salek, M. M., Carrara, F., Zhou, J., Stocker, R., & Jimenez-Martinez, J. (2024). Multiscale porosity microfluidics to study bacterial transport in heterogeneous chemical landscapes. *Advanced Science*, *11*(20), 2310121. https://doi.org/10.1002/advs.202310121

Sangani, A. S., & Acrivos, A. (1983). The effective conductivity of a periodic array of spheres. *Proceedings of the Royal Society of London. A. Mathematical and Physical Sciences*, *386*(1791), 263–275. https://doi.org/10.1098/rspa.1983.0036

Sanquer, H., Heyman, J., Hanna, K., & Le Borgne, T. (2024). Microscale chaotic mixing as a driver for chemical reactions in porous media. *Environmental Science & Technology*, *58*(20), 8899–8908. https://doi.org/10.1021/acs.est.3c09749

Selroos, J.-O., & Cvetkovic, V. (1992). Modeling solute advection coupled with sorption kinetics in heterogeneous formations. *Water Resources Research*, *28*(5), 1271–1278. https://doi.org/10.1029/92WR00011

Silliman, S. E. (2001). Laboratory study of chemical transport to wells within heterogeneous porous media. *Water Resources Research*, *37*(7), 1883–1892. https://doi.org/10.1029/2001wr900005

Silliman, S. E., & Simpson, E. S. (1987). Laboratory evidence of the scale effect in dispersion of solutes in porous media. *Water Resources Research*, *23*(8), 1667–1673. https://doi.org/10.1029/WR023i008p01667

Soltanmohammadi, R., Iraji, S., De Almeida, T. R., Basso, M., Munoz, E. R., & Vidal, A. C. (2024). Investigation of pore geometry influence on fluid flow in heterogeneous porous media: A pore-scale study. *Energy Geoscience*, *5*(1), 100222. https://doi.org/10.1016/j.engeos.2023.100222

Souzy, M., Lhuissier, H., Méheust, Y., Le Borgne, T., & Metzger, B. (2020). Velocity distributions, dispersion and stretching in three-dimensional porous media. *Journal of Fluid Mechanics*, *891*, A16. https://doi.org/10.1017/jfm.2020.113

Tatti, F., Papini, M. P., Sappa, G., Raboni, M., Arjmand, F., & Viotti, P. (2018). Contaminant back-diffusion from low-permeability layers as affected by groundwater velocity: A laboratory investigation by box model and image analysis. *Science of the Total Environment*, *622–623*, 164–171. https://doi.org/10.1016/j.scitotenv.2017.11.347

Trefry, M. G., Lester, D. R., Metcalfe, G., Ord, A., & Regenauer-Lieb, K. (2012). Toward enhanced subsurface intervention methods using chaotic advection. *Journal of Contaminant Hydrology*, *127*(1), 15–29. (GQ10: Groundwater Quality Management in a Rapidly Changing World). https://doi.org/10.1016/j.jconhyd.2011.04.006

Trefry, M. G., McLaughlin, D., Lester, D. R., Metcalfe, G., Johnston, C. D., & Ord, A. (2011). Stochastic relationships for periodic responses in randomly heterogeneous aquifers. *Water Resources Research*, *47*(8). https://doi.org/10.1029/2011WR010444

Turuban, R., Lester, D. R., Le Borgne, T., & Méheust, Y. (2018). Space-group symmetries generate chaotic fluid advection in crystalline granular media. *Physical Review Letters*, *120*(2), 024501. https://doi.org/10.1103/PhysRevLett.120.024501

Uffink, G., Elfeki, A., Dekking, M., Bruining, J., & Kraaikamp, C. (2012). Understanding the non-gaussian nature of linear reactive solute transport in 1D and 2D: From particle dynamics to the partial differential equations. *Transport in Porous Media*, *91*(2), 547–571. https://doi.org/10.1007/s11242-011-9859-x

van Beinum, W., Meeussen, J. C., Edwards, A. C., & van Riemsdijk, W. H. (2000). Transport of ions in physically heterogeneous systems; convection and diffusion in a column filled with alginate gel beads, predicted by a two-region model. *Water Research*, *34*(7), 2043–2050. https://doi.org/10.1016/S0043-1354(99)00371-1

Van Beinum, W., Meeussen, J. C., & Van Riemsdijk, W. H. (2000). Modeling transport of protons and calcium ions in an alginate gel bead system: The effects of physical nonequilibrium and nonlinear competitive sorption. *Environmental Science & Technology*, *34*(23), 4902–4907. https://doi.org/10.1021/es000018

Van Rossum, G., & Drake, F. L. (2009). *Python 3 reference manual*. CreateSpace.

Varghese, J. S., Chellappa, N., & Fathima, N. N. (2014). Gelatin–carrageenan hydrogels: Role of pore size distribution on drug delivery process. *Colloids and Surfaces B: Biointerfaces*, *113*, 346–351. https://doi.org/10.1016/j.colsurfb.2013.08.049

Verma, N. K., Singh, A. K., Yadav, V., Singh, P., Yadav, A., & Jaiswal, S. (2021). Super porous hydrogel based drug delivery system: A review. *South Asian Research Journal of Pharmaceutical Sciences*, *3*(6), 103. https://doi.org/10.36346/sarjps.2021.v03i06.004

Virtanen, P., Gommers, R., Oliphant, T. E., Haberland, M., Reddy, T., Cournapeau, D., & SciPy 1.0 Contributors. (2020). SciPy 1.0: Fundamental algorithms for scientific computing in python. *Nature Methods*, *17*(3), 261–272. https://doi.org/10.1038/s41592-019-0686-2

Wright, E. E., Richter, D. H., & Bolster, D. (2017). Effects of incomplete mixing on reactive transport in flows through heterogeneous porous media. *Physical Review Fluids*, *2*(11), 114501. https://doi.org/10.1103/PhysRevFluids.2.114501

Ye, Y., Chiogna, G., Cirpka, O., Grathwohl, P., & Rolle, M. (2015). Experimental investigation of compound-specific dilution of solute plumes in saturated porous media: 2-d vs. 3-d flow-through systems. *Journal of Contaminant Hydrology*, *172*, 33–47. https://doi.org/10.1016/j.jconhyd.2014.11.002

Yuan, N., Zhao, A., Hu, Z., Tan, K., & Zhang, J. (2022). Preparation and application of porous materials from coal gasification slag for wastewater treatment: A review. *Chemosphere*, *287*, 132227. https://doi.org/10.1016/j.chemosphere.2021.132227

Yuan, T., Shen, L., & Dini, D. (2024). Porosity-permeability tensor relationship of closely and randomly packed fibrous biomaterials and biological tissues: Application to the brain white matter. *Acta Biomaterialia*, *173*, 123–134. https://doi.org/10.1016/j.actbio.2023.11.007

Zakirov, T. R., & Khramchenkov, M. G. (2022). Effect of pore space heterogeneity on the adsorption dynamics in porous media at various convection-diffusion and reaction conditions: A lattice Boltzmann study. *Journal of Petroleum Science and Engineering*, *212*, 110300. https://doi.org/10.1016/j.petrol.2022.110300

Zhang, W., Wang, L., Chen, J., & Zhang, Y. (2024). Preferential flow in soils: Review of role in soil carbon dynamics, assessment of characteristics, and performance in ecosystems. *Eurasian Soil Science*, *57*(5), 1–12. https://doi.org/10.1134/s1064229323602548

Zhang, Y., He, S.-Y., Wang, P., Gu, J., Jiang, Q., Liu, M., & Wen, C. (2024). Impacts of permeability and effective diffusivity of porous scaffolds on bone ingrowth: In silico and in vivo analyses. *Biomaterials Advances*, *161*, 213901. https://doi.org/10.1016/j.bioadv.2024.213901

Zhang, Z., Zhang, Z., Lu, W., Guo, H., Liu, C., & Ning, F. (2024). Pore-scale investigations of permeability of saturated porous media: Pore structure efficiency. *Journal of Hydrology*, *637*, 131441. https://doi.org/10.1016/j.jhydrol.2024.131441

Zhao, F., Vaughan, T. J., & McNamara, L. M. (2016). Quantification of fluid shear stress in bone tissue engineering scaffolds with spherical and cubical pore architectures. *Biomechanics and Modeling in Mechanobiology*, *15*(3), 561–577. https://doi.org/10.1007/s10237-015-0710-0

Ziliotto, F., Basilio Hazas, M., Muhr, M., Ahmadi, N., Rolle, M., & Chiogna, G. (2025). Relevance of local dispersion on mixing enhancement in engineering injection and extraction systems in porous media: Insights from laboratory bench-scale experiments and modeling. *Transport in Porous Media*, *152*(3), 20. https://doi.org/10.1007/s11242-025-02155-7